

The magnetic fields of intermediate-mass T Tauri stars : I. Magnetic detections and fundamental stellar parameters

F. VILLEBRUN¹, E. ALECIAN¹, G. HUSSAIN^{2,3}, J. BOUVIER¹, C. P. FOLSOM³, Y. LEBRETON^{4,5}, L. AMARD¹⁰, C. CHARBONNEL^{3,6},
F. GALLET^{1,6}, L. HAEMMERLÉ⁶, T. BÖHM³, C. JOHNS-KRULL⁷, O. KOCHUKHOV⁸, S. C. MARSDEN⁹, J. MORIN¹¹, and P. PETIT³

¹ Université Grenoble Alpes, CNRS, IPAG, F-38000 Grenoble, France, e-mail: florent.villebrun@univ-grenoble-alpes.fr

² European Southern Observatory, Karl-Schwarzschild-Str. 2, D-85748 Garching bei München, Germany

³ IRAP, Université de Toulouse, CNRS, CNES, UPS, F-31400 Toulouse, France

⁴ LESIA, Observatoire de Paris, PSL Research University, CNRS UMR 8109, 5 Place Jules Janssen, F-92195 Meudon, France

⁵ Institut de Physique de Rennes, Université de Rennes 1, CNRS UMR 6251, F-35042 Rennes, France

⁶ Department of Astronomy, University of Geneva, Chemin des Maillettes 51, 1290 Versoix, Switzerland

⁷ Department of Physics & Astronomy, Rice University, 6100 Main Street, MS-108, Houston, TX 77005, USA

⁸ Department of Physics and Astronomy, Uppsala University, Box 516, 75120 Uppsala, Sweden

⁹ University of Southern Queensland, Centre for Astrophysics, West Street, Toowoomba, QLD 4350, Australia

¹⁰ University of Exeter, Department of Physics & Astronomy, Stoker Road, Devon, Exeter, EX4 4QL, UK

¹¹ LUPM, Université de Montpellier & CNRS, Montpellier, Cedex 05, France

Received xxxxxxxx 2018

ABSTRACT

Context. The origin of the fossil magnetic fields detected in 5 to 10% of intermediate-mass main sequence stars is still highly debated. **Aims.** We want to bring observational constraints to a large population of intermediate-mass pre-main sequence (PMS) stars in order to test the theory that convective-dynamo fields generated during the PMS phases of stellar evolution can occasionally relax into fossil fields on the main sequence.

Methods. Using distance estimations, photometric measurements, and spectropolarimetric data from HARPSpol and ESPaDOnS of 38 intermediate-mass PMS stars, we determined fundamental stellar parameters (T_{eff} , L and $v \sin i$) and measured surface magnetic field characteristics (including detection limits for non-detections, and longitudinal fields and basic topologies for positive detections). Using PMS evolutionary models, we determined the mass, radius, and internal structure of these stars. We compared different PMS models to check that our determinations were not model-dependant. We then compared the magnetic characteristics of our sample accounting for their stellar parameters and internal structures.

Results. We detect magnetic fields in about half of our sample. About 90% of the magnetic stars have outer convective envelopes larger than $\sim 25\%$ of the stellar radii, and heavier than $\sim 2\%$ of the stellar mass. Going to higher mass, we find that the magnetic incidence in intermediate-mass stars drops very quickly, within a time-scale of the order of few times 0.1 Myr. Finally, we propose that intermediate-mass T Tauri stars with large convective envelopes, close to the fully convective limit, have complex fields and that their dipole component strengths may decrease as the sizes of their convective envelopes decrease, similar to lower-mass T Tauri stars.

Key words. stars: variables: T Tauri, Herbig Ae/Be, stars: activity - fundamental parameters - magnetic field - pre main sequence

1. Introduction

A very peculiar type of magnetic field can be found in 5 to 10% of Herbig Ae/Be (HAeBe) and A/B stars: a very strong field (300 - 30kG), stable over many years and even decades, and that tends to be dominated by low-order largely dipolar large-scale fields (Alecian et al. 2013; Donati & Landstreet 2009). The other 90 - 95% of HAeBe and A/B stars do not host magnetic fields, or at least they are not detected. As these stars do not have a convective envelope, the dynamo process (that usually explains the presence and the characteristics of magnetic fields in cooler stars) cannot be invoked to explain either the presence or the characteristics of the fields observed in HAeBe and A/B stars. In addition, the dynamo field formed in the core of intermediate mass stars on or very near the main sequence would take too long to rise to the surface (e.g. Moss 2001) raising the need for an al-

ternative explanation for the presence of such magnetic fields in intermediate-mass stars.

The underlying mechanisms causing these fields in non-convective stars is unclear and the debate centres around two theories, both of which implying that the magnetic fields come from earlier evolutionary stages of the stars, leading people to call these "fossil fields". The first theory consists of frozen-in magnetic fields originally present in the interstellar medium during the collapse of the pre-stellar cloud (Moss 2001), while the other consists of relaxing the dynamo field that is created during the pre-main sequence (PMS) convective phase in stars that meet specific conditions related to their rotation (Duez & Mathis 2010; Braithwaite & Spruit 2004; Emeriau & Mathis 2015; Gaurat et al. 2015). In this paper, we will not focus on the first scenario, and will instead derive new observational constraints to the second scenario by measuring the rotational and magnetic properties of HAeBe and A/B stars' progenitors: the intermediate-mass T Tauri stars (IMTTS). Because IMTTS correspond to the very last convective stage of intermediate-mass

Send offprint requests to: F. Villebrun, e-mail: florent.villebrun@univ-grenoble-alpes.fr

stars (i.e. before they lose their convective envelopes to become fully radiative), they are the best objects to study to test the relaxation scenario.

T Tauri stars (TTS) are PMS stars with spectral types between late F and M that are gravitationally contracting while evolving towards the main sequence (Herbig 1962). Some of them possess circumstellar disks, and many are still actively accreting. Intermediate-mass T Tauri stars (1.2 to 4 M_{\odot}) are precursors to HAeBe stars, and later to A/B stars. Studies of 16 low-mass T Tauri stars (LMTTS) have revealed that - unlike in HAeBe stars - magnetic fields are ubiquitous in these systems and of dynamo type (Donati et al. 2008, 2010b, 2011a, also see Hill et al. 2017 for a summary of all the results to date). Hussain et al. (2009) detected and reconstructed the large-scale surface magnetic fields in 2 IMTTS (CV Cha and CR Cha), but aside from this work, no other surface magnetic field maps of IMTTS have been published. Our knowledge of IMTTS magnetic properties is therefore very limited.

To test the relaxation theory we need to determine the magnetic topologies and strengths of a sample of IMTTS well distributed among the PMS phase from their fully convective to fully radiative evolutionary stages. In particular, we need to determine the ratio between poloidal and toroidal fields (Emeriau & Mathis 2015, Mathis private communication), which is only accessible with ZDI (Zeeman Doppler Imaging) magnetic mapping (e.g. Hussain et al. 2009). As this technique requires continuous monitoring, evenly sampling at least one stellar rotation period, a considerable investment of telescope time is needed for each star. We therefore need to filter out the most suitable targets for mapping, i.e. those with strong large-scale magnetic fields. To this end, we selected a set of targets aiming to cover the part of the HR diagram that corresponds to IMTTS as thoroughly as possible. Future observations to obtain full ZDI maps for a small subset of the sample with the strongest magnetic fields will be reported in a subsequent paper.

Here, we report the initial step in our programme, an observational campaign of a large sample of IMTTS using ESPaDOnS (at the Canada France Hawaii Telescope, CFHT) and HARPSpol (at ESO La Silla) to acquire a few high-resolution spectropolarimetric observations per star (Section 2). We used these data to detect magnetic fields, and to determine the effective temperature of our sample consistently and as accurately as possible (Section 3). For the first time, we have therefore been able to place accurately these stars in the HR diagram, and compare their positions with PMS evolutionary tracks computed using different models, to predict their internal structure (Section 3). We discuss our results and present our conclusions in Sections 4 and 5, respectively.

2. Observations

We based this study on 92 spectra for 38 IMTTS we obtained in 2012. For each star, we acquired up to 4 spectra. These spectra have been obtained with either the ESPaDOnS or HARPSpol instruments. ESPaDOnS is a high-resolution spectropolarimeter, and has been used in the polarimetric Stokes V mode (Donati 2003). It is located at the CFHT and has a spectral resolution $R = 65000$ (its wavelength range covers between 369 nm and 1048 nm). HARPSpol is the polarimetric module of the HARPS spectrograph (Piskunov et al. 2011) located at La Silla observatory, Chile (ESO 3.6m), which has a spectral resolution $R = 115000$ (its wavelength range covers between 378 nm and 691 nm). For both instruments, the circular polarisation state of the stellar light is obtained by acquiring 4 successive spectra at

different phase retarder configurations. The data have been reduced using Libre-ESPRIT when obtained with ESPaDOnS, and the REDUCE package adapted for HARPSpol (e.g. Alecian et al. 2011). Libre-ESPRIT is based on the earlier ESPRIT (Donati et al. 1997) and uses the same basic reduction methods. Some spectra from HARPSpol were also reduced by Libre-ESPRIT to double-check the reduced spectra. From this data reduction, we get one Stokes I and one Stokes V spectrum per observation, as well as one diagnostic spectrum (null-spectrum or N-spectrum, see Donati et al. 1997) where the data are combined in such a way to cancel stellar polarization signal. This null-spectrum enables us to make sure the polarized light we acquire does not come from spurious origins (e.g., instrumental or observing conditions). The median signal-to-noise ratio (SNR) of our data is 170 at peak per CCD pixel for one observation (for fainter sources, one observation could consist of several successive Stokes V sequences). A log of the observations can be found in Table B.1.

The normalisation provided by the data reduction pipelines being insufficient for our work, we used a polynomial renormalisation routine (Folsom et al. 2008, 2012). This routine determines continuum points in the stellar spectrum order by order, and then fits a polynomial function based on these continuum points. The original spectrum is then divided by the fitted polynomial function, making sure that the spectrum is properly normalised.

In order to increase the SNR of our data, we built the mean Least-Squares Deconvolved (LSD) profiles of our spectra as described in Donati et al. (1997). For all of the stars, the LSD profiles have been normalized using a mean wavelength of 500 nm and a mean Landé factor of 1.2 (Kochukhov et al. 2010). For each star, a tailored list of atomic lines parameters, called a line-mask, is compiled from a synthetic spectrum created with the effective temperature, and $\log g$ (determined in Section 3). We used solar abundances which are appropriate for our sample (see Section 3). We used the Vienna Atomic Line Database (VALD3 version, Ryabchikova et al. 2015) to build the line-masks, and excluded from these masks spectral regions affected by Balmer lines, emission lines, telluric lines, and regions with a poor SNR.

3. Results

3.1. Stellar properties

We want to determine stellar properties of our sample to better constrain their position in the HR diagram and better understand their magnetic behaviour in terms of their effective temperature and internal structure.

3.1.1. Effective temperatures and rotational velocities

To derive the effective temperature, T_{eff} , and projected rotational velocities, $v \sin i$, of these stars, we used the spectral fitting method: for each observed spectrum, we created an associated synthetic spectrum using the ZEEMAN code (Landstreet 1988; Wade et al. 2001; Folsom et al. 2012) that, according to a χ^2 -fitting procedure, best fits the observed spectrum. We used a grid of stellar atmospheric models from the MARCS code (Gustafsson et al. 2008) using global solar abundances from Asplund et al. (2009). Model atmospheres were interpolated between grid points, using linear interpolation of the log of the model quantities, to obtain exact T_{eff} and $\log g$ combinations. Atomic data were extracted from the VALD3 database using "extract stellar"

requests with parameters corresponding to the range of stellar parameters of interest.

We first needed initial estimates of the star's fundamental parameters (v_{rad} , T_{eff} , $v \sin i$ and v_{mac}) which we determined by eye using the IDL visualisation script BINMAG2¹ (see Alecian et al. 2016). These first estimates of fundamental stellar parameters are then used by the LMA semi-automatic routine (Folsom et al. 2012) as a starting point for a χ^2 minimisation using the Levenberg-Marquardt technique. Synthetic spectra are created by the ZEEMAN spectrum synthesis code and compared to the observed spectrum until all free parameters converge to their optimal solution. The free parameters in this fitting procedure are: T_{eff} , $v \sin i$, the microturbulence velocity v_{mic} , and the radial velocity v_{rad} . We fixed $\log g$ to 4.0 as our data were of variable quality – the ability to determine $\log g$ depends on both $v \sin i$ and the SNR of the spectrum – and so this quantity could not be consistently determined across the entire sample. $\log g = 4.0$ is a reasonable value for the part of the Hertzsprung-Russell diagram (HRD) covered by our sample. We used global solar metallicity from Asplund et al. (2009) and found that they reproduce our data well: there was therefore no need to fit the abundances as well. We also fixed the macro-turbulent velocity, v_{mac} , to 2.0 km s^{-1} as it reproduces well our data for low $v \sin i$ stars, and could not be constrained for high $v \sin i$ stars (as the rotation dominates line broadening).

We took into account the broadest possible spectral range, but had to discard several wavelength windows that were strongly affected by telluric absorption lines, or night sky or YSO emission lines. We also had to discard the blue part of the spectra (i.e. $\lambda < 400 \text{ nm}$) because noise is high and blending with Balmer lines becomes severe. As a result of this filtering, we fitted 12 wavelength windows for ESPaDOnS spectra ($\sim 90 \text{ nm}$ per window, totaling 1085 nm) and 10 wavelength windows for HARPSpol spectra (totaling 885 nm). For each window, we produced an estimate of T_{eff} and $v \sin i$. We then averaged all the values of T_{eff} and $v \sin i$ for all the windows of a single spectrum in order to obtain a preliminary estimate of T_{eff} and $v \sin i$ for the entire spectrum. To discard potential bad fits, we excluded the windows that deviated from the mean value by 1σ , excluded them, and re-calculated a new average. We did this operation only once: this 1σ -clipping resulted in the exclusion of 1 or 2 windows in most cases, and up to 4 or 5 windows at the most (for spectra that were noisier than the rest and / or for fast rotating stars). Following this procedure, we derived T_{eff} and $v \sin i$ with standard deviations of the mean of 100-150 K and $1-2 \text{ km s}^{-1}$ respectively (450 K and 20 km s^{-1} for the most challenging case, i.e. for spectra that were noisier than the rest and / or for fast rotating stars). All these results are compiled in Table B.2.

Some stars of our sample may still be strongly accreting. We therefore checked for the presence of veiling by comparing the measured T_{eff} at high and low wavelengths (i.e. in the red and blue parts of the spectra respectively). Because accretion shocks emit more radiations (relative to photospheres) in the blue / UV part of the spectra, the calculated T_{eff} may be over-estimated at shorter wavelengths: the lines are shallower due to an extra continuum contribution from accretion hot spots at or near the stellar surface. Except for 3 stars, no significant veiling was found in our sample. For the three affected by veiling (V1000 Sco, V1152 Sco and V1156 Sco), the T_{eff} was consistently higher in the blue by 400-500 K. In these cases, it is more cautious to ignore the calculated T_{eff} in the blue part, and only consider the calculated T_{eff} in the red part (as it is less affected by veiling).

Thanks to the 1σ -clipping, these abnormally high T_{eff} estimates have been excluded, and the final temperatures of these 3 stars are largely based on the temperatures found in their red spectral windows ($>580 \text{ nm}$). We thus are confident that veiling did not significantly skew our T_{eff} determination.

3.1.2. Luminosities

To position our sample of IMTTS in the HR diagram, we needed to compute their luminosities, which first requires the determination of the extinction. We based our determination of A_J on the $(V - J)$ color, $(B - V)$ being more affected by accretion and circumstellar extinction. We looked for the most consistent photometric measurements available in the literature. In most cases, we used the J magnitudes from the 2MASS survey (Cutri et al. 2003) and V magnitudes from Kharchenko (2001) or the NOMAD catalogue (Zacharias et al. 2004). Using our determination of effective temperature, we derived the associated empirical $(V - J)_0$ of 5-30 Myr intermediate-mass stars from Pecaut & Mamajek (2013) to compute the color excesses $E(V - J)$ and extinctions A_J . The total to selective extinction $R_J=0.437$ has been determined from the color excesses and extinctions found in Casagrande et al. (2010) following the relationship:

$$\frac{R_J}{R_V} \times \frac{E(V - J)}{E(B - V)} = \frac{A_J}{A_V} \quad (1)$$

We used the distance from Tycho-Gaia Astrometric Solution (TGAS, Gaia Collaboration et al. 2016) whenever available in order to determine the absolute magnitudes M_J . However, for half of the stars, TGAS distances were not yet available: we thus used the best distance estimate of their associated star-forming region or cluster found in the literature (see Table B.3 for distance estimates). We then used bolometric corrections $(BC)_J$ from Pecaut & Mamajek (2013) to get their bolometric magnitudes, and finally determined the bolometric luminosities using a solar bolometric absolute magnitude of 4.755, also from Pecaut & Mamajek (2013). All the informations about the magnitudes and luminosities of our sample are compiled in Table B.4.

When trying to determine the bolometric luminosities of NGC 6530 SCB 7 and NGC 6530 SCB 739, we found abnormally high values ($\log(L/L_\odot) = 2.55$ and 3.16 , respectively). Because of these very high luminosities, these 2 stars are far above the birthline, which is impossible according to standard PMS theory. These errors might have the following causes: the first one being they are not pre-MS but post-MS stars, the second one being bad photometric measurements (for both of them, the $B - V - J$ magnitude measurements are reported with "C" or even "D" flags on SIMBAD, meaning we should be cautious when using them), and the third one being bad estimates of their distances. We favour the third scenario: there are no GAIA parallaxes for these 2 stars, and thus we adopted the distance of NGC 6530 from Sung et al. (2000). As these 2 stars are poorly studied, we suspect NGC 6530 SCB 7 and NGC 6530 SCB 739 of actually being in front of NGC 6530, explaining why the bolometric luminosity of these 2 stars is highly overestimated². Despite their luminosities being undetermined, it does not affect our determination of their effective temperatures, rotational velocities, and magnetic fields reported in this paper.

² In the meanwhile, GAIA DR2 distances (??) have been released for the two stars. They confirm these stars are very much in the foreground.

¹ see the webpage <http://www.astro.uu.se/~oleg/binmag.html>

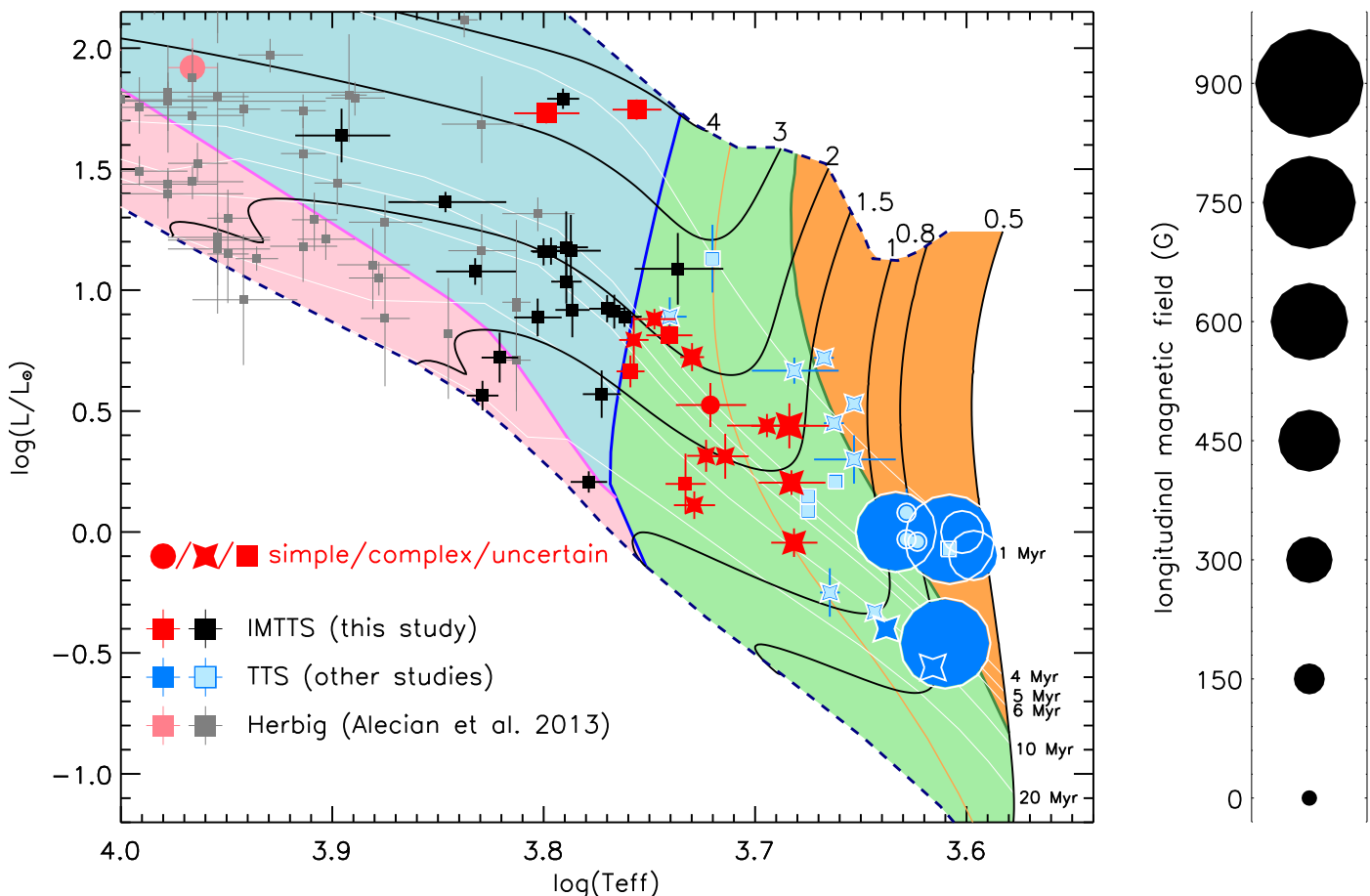


Fig. 1. HR diagram compiling the positions of IMTTS from this study (red and black symbols), and of IMTTS and LMTTS (blue symbols), and HAeBes (faded symbols) from other studies. Black and gray symbols are stars in which no magnetic field has been detected. Red and blue symbols are stars for which a magnetic field has been detected: stars represent complex magnetic topologies, circles represent simple magnetic topologies, and squares represent undefined magnetic topologies. The sizes of the red and dark blue symbols are proportional to the maximum absolute value of the longitudinal magnetic field measurements for each star. A light blue symbol means no such measurement is available. The youngest magnetic HAeBe star (HD 190073) is indicated on the top-left corner as an isolated red circle. The shaded areas have the following meaning; orange: fully convective; green: radiative core + convective envelope; blue: fully radiative; and pink: convective core + radiative envelope. The evolutionary tracks (solid black line, ranging from 1.0 - 4.0 M_{\odot}), isochrones (solid white line) and ZAMS (lower dashed line) are from the CESAM code, while the birthline (upper dashed line) is from Behrend & Maeder (2001). The numbers above each evolutionary track are the stellar mass in **solar units**. The numbers beside each isochron is the stellar age. The thin orange line is the location where $R_{\text{conv.env.}}/R_{\star} = 40\%$.

3.1.3. Mass, radius, convective turnover time, and internal structure

We now want to determine other stellar parameters using PMS evolutionary models. To estimate the uncertainties introduced by these models, we compared 3 different grids of models that can be applied to the IMTTS mass range and calculated with 3 different stellar evolution codes: the CESAM code (Morel & Lebreton 2008; Marques et al. 2013), the STAREVOL code (Palacios et al. 2003; Lagarde et al. 2012; Amard et al. 2016), and the Geneva code (Eggenberger et al. 2008, Haemmerlé 2014 PhD thesis). More details about these 3 sets of models and their comparison can be found in Appendix A and Fig A.1 at the end of this paper. We concluded that these 3 PMS models were similar enough -in the region of the HRD considered here and within the errors of our measurements of T_{eff} and $\log(L)$ - and confirm any of them can be used for our study. We decided to use the CESAM code, for practical reasons.

The resulting positions of the stars of our sample in the HR diagram are plotted in Fig. 1. From these, we interpolated stellar parameters that cannot be directly determined from spectropolarimetric observations: i.e. stellar mass, radius, convective turnover time τ_c (calculated at half a pressure scale height above the base of the convective envelope $H_p/2$, as described in Charbonnel et al. (2017)), and the mass and radius of the convective and radiative zones. We need to constrain all these parameters in order to test the magnetic field relaxation scenario. The procedure we used to interpolate these parameters is similar to the one described in Alecian et al. (2009). All these results can be found in Table B.2.

3.2. Magnetic properties

We now want to determine which stars of our sample are magnetic, and for those that are we want to determine their magnetic field properties (strengths and topologies).

3.2.1. Magnetic field detections

From the Stokes V profile of each spectrum, we computed the false alarm probability (FAP, Donati et al. 1997). The detection of a magnetic field by the FAP is based on a comparison between the Stokes V profile and the noise. We consider that a star hosts a magnetic field if we get at least one definite detection in one observation, as defined by Donati et al. (1997). In addition, we checked that the null-spectra are flat for all our observations, and found no evidence for a spurious contribution to the Stokes V profiles. We find that 18 stars out of our entire sample host a magnetic field, and we have no significant detections for the remaining 20 stars.

We then measured the line-of-sight component of the magnetic field averaged over the visible stellar hemisphere: the mean longitudinal magnetic field (B_ℓ , e.g. Rees & Semel 1979; Kochukhov et al. 2010). B_ℓ is measured by dividing the first moment of the Stokes V profile by the equivalent width of the Stokes I profile, and multiply this ratio by a factor that depends on the mean wavelength and mean Landé factor used for the normalisation of the LSD profile (Section 2). In Table B.5 are reported the B_ℓ and associated σ_{B_ℓ} of each observation, for both magnetic and non-magnetic stars.

One might worry that, on average, all the stars for which we do not detect a magnetic field are just more difficult to detect a field on because they are rotating faster. To address this, we plotted the σ_{B_ℓ} of each spectrum with respect to the rotational velocity of its associated star in Fig. 2. Red dots are for spectra coming from magnetic stars, and black dots are for spectra coming from stars with no magnetic detection. For $v \sin i$ up to 80 km/s (which concerns 33 stars out of 38), Fig. 2 shows that we can reliably detect magnetic fields with our data. Beyond this limit (concerning 5 stars) we did not detect any magnetic field: we therefore may be biased by fast rotation when above 80 km/s, but it also may be possible that none of these 5 stars actually host a strong large-scale magnetic field.

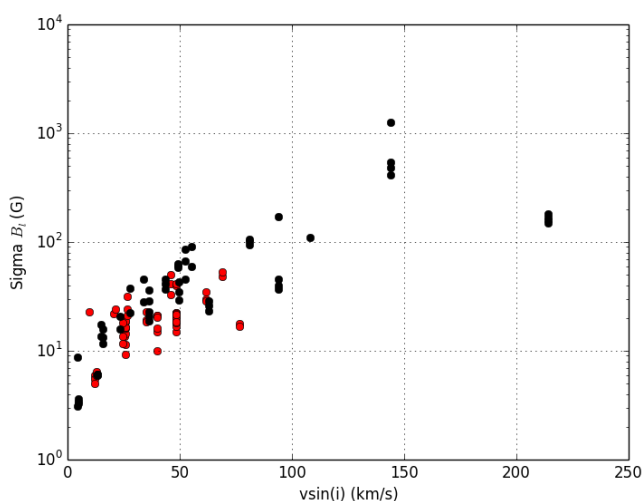


Fig. 2. σ_{B_ℓ} of each observation, with respect to the $v \sin i$ of its associated star. Red dots are for spectra coming from magnetic stars, black dots are for spectra coming from stars with no detected magnetic field.

3.2.2. Limits of detection for a dipolar configuration

When we did not find any evidence of a magnetic field in a star, we computed an upper limit for the detection of a dipolar field configuration. Considering the case that the star hosts a dipolar magnetic field (i.e. the configuration commonly found in fossil field stars and in some cool stars possessing a field that is not fossil; e.g. Petit et al. 2008; Morin et al. 2010; Boro Saikia et al. 2016), we estimated the maximum strength below which the hypothetical dipolar field could not have been detected in our data, according to the SNR of our observations. The calculation of this limit is carried out by a Monte-Carlo simulation.

We followed the same procedure as described in Alecian et al. (2016): for 15 values of a hypothetical dipolar magnetic field strengths B_D ranging from 0 to 5000 G, we created 1000 synthetic V profiles, each of which was associated to a randomly generated oblique rotator configuration (random inclination angle to the observer i , random obliquity angle of the dipole β , and random rotational phase of the star ϕ). For each of these configurations, we computed the FAP in the synthetic Stokes V profile (after adding synthetic noise with respect to the quality of our observations) to decide if a magnetic field of strength B_D would have been detected, using the same detection criteria as in our observations and detailed in the previous section. After 1000 trials, we can therefore give a detection probability for a dipolar field of strength B_D at its pole. We set our detection threshold at 95%, meaning that the value $B_{D95\%}$ mentioned in Table 6 is the value of B_D for which the synthetic magnetic field has been detected in 95% of the trials. Having more than one observation for a star is beneficial as it gives us more chances to detect a magnetic field: we consider all the different observations we got as independant draws, and can therefore combine the detection probabilities to improve our limit of detection.

The values of $B_{D95\%}$ for the 20 non-magnetic stars are plotted in Fig. 3 : we observe that $B_{D95\%}$ is lower than 500 G for half of our non-magnetic stars, and lower than 1 kG for 80% of them. We also observe a correlation between $B_{D95\%}$ and $v \sin i$. Indeed, rotational broadening may hide magnetic signatures by spreading them over more spectral pixels, reducing the amplitude of the magnetic signature relative to the noise. For example, the very high rotational velocity of NGC 2264 121 ($v \sin i = 144 \text{ km s}^{-1}$) is partly responsible for its very high detection limit (5200 G). We would need to observe this target for much longer to increase significantly the SNR and give us a chance to detect a field of lower strength.

3.2.3. Limits of detection for a multipolar configuration

We initially computed the limits of detection in the case of a dipolar field for our stars in which there are no detections, as this is the typical configuration in fossil fields stars. However, the non-magnetic stars of our sample may also hide a multipolar field (or a multipolar+toroidal field, more typical of cool active stars). We investigated whether or not these stars could host complex, large-scale magnetic field signatures of the type found in the IMTTS CV Cha (Hussain et al. 2009). We used the published map of CV Cha to predict the Stokes V signatures expected in each of the stars with non-detections. As the large-scale field is complex and multipolar, the main factors determining whether or not the signatures are likely to be detected are the stellar $v \sin i$ and the SNR levels of the LSD Stokes V profile. By randomly sampling hundreds of phases for each star, we can assign the probability of detecting a CV Cha-type complex multipolar field at the $3\text{-}\sigma$ level. The results are shown in the third column of

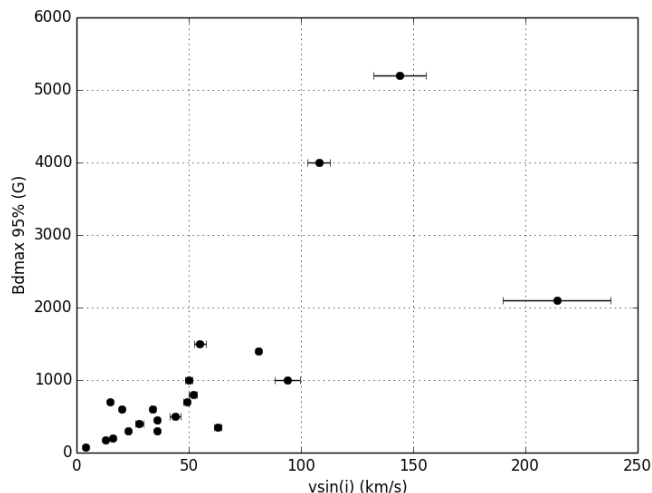


Fig. 3. Limit of detection for a dipolar magnetic field at the 95% confidence for the 20 non-magnetic stars of our sample versus the projected rotational velocities of these stars.

Table 6. Stars with no-detected magnetic field: upper-limit of detection in the case of a dipolar field ($B_{D95\%}$, second row) and 3 – σ level probability of detecting complex, large-scale magnetic field signatures of CV Cha-type ($P_{3-\sigma}$, third row).

Target	$B_{D95\%}$ (G)	$P_{3-\sigma}$
BN Ori	2100	0
CQ Tau	1000	19
HD 135127	4000	0
HD 137059	400	82
HD 143978	300	95
IRAS 22152+6947	500	66
NGC 2264 108	800	33
NGC 2264 121	5200	0
NGC 2264 84	450	84
NGC 6530 SCB739	70	100
PAR 102	700	11
PAR 1391	700	88
PAR 1394	350	86
PAR 1414	600	58
PAR 1455	300	88
PAR 1646	200	90
PAR 1736	1500	5
PAR 2441	180	100
PX Vul	1400	0
RY Ori	1000	62

Table 6, which shows the percentage probability of detecting a field, given the stellar parameters and the data quality. Our findings suggest that a complex multipolar field signature typical of partly-convective T Tauri stars should definitely have been detected for NGC 6530 SCB 739 and Par 2441 (though we cannot exclude a significantly weaker field). For HD 143978, a robust field signature would be expected approximately 95% of the time. For the rest of the sample, we cannot exclude the possibility that these stars host complex fields such as those found in the CV Cha and CR Cha.

4. Discussion

4.1. The origin of magnetic fields in Herbig and Ap stars

We want to understand the evolution of the magnetic properties of intermediate-mass stars from the birthline to the Herbig phase, which necessitates a knowledge of the magnetic proper-

ties of the intermediate-mass T Tauri stars, the thus far poorly studied evolutionary precursors of the Herbig Ae/Be stars. We have performed an observational campaign of a specific sample of IMTTS evolving from a fully convective structure to a fully radiative structure. The stars of our sample are plotted in Fig. 1 with red symbols when we obtained a magnetic detection (16 stars in Fig. 1 + 1 falling out of the HRD, see Sect. 3.1.2.), and black symbols when no magnetic field has been detected (19 stars in Fig. 1 + 1 falling out of the HRD, see Sect. 3.1.2.). The sizes of the symbols depend on the maximum strength of our B_ℓ measurements (the minimum sizes being for the non-magnetic stars).

We have divided the HRD in 4 different zones. In Fig. 1., the orange zone indicates the position of the stars evolving with a fully convective interior. The green zone indicates partly-convective stars, i.e. stars with a radiative core larger than 1% of the stellar radius R_\star (equivalent to 1% of the stellar mass M_\star), and lower than 75% R_\star (or 98% M_\star). The blue zone, called the fully-radiative zone, contains stars with a radiative core containing more than 98% of the stellar mass, and the pink region are for stars in which a convective core is growing and has a mass larger than 1% M_\star .

In order to complete the global picture, we included stars from other spectro-polarimetric studies in Fig. 1: Herbig Ae/Be stars from Alecian et al. (2013) – using similar symbols as the IMTTS but with faded colours; as well as other IMTTS and LMTTS – using blue symbols (Donati et al. 2007, 2008, 2010a, 2011b,c, 2013, 2015; Hussain et al. 2009; Kochukhov 2015; Hill et al. 2017; Lavail et al. 2017; Yu & Donati 2017). In the latter case, all stars are magnetic, and the light-blue (blue) colour indicates a lack (or not) of information on the B_ℓ values. We observe that, while the fully-convective zone above $\sim 1 M_\odot$ is almost empty, our sample bridges well the gap between the fully convective and fully-radiative zones at intermediate-mass.

In the fully radiative part of the HR diagram (blue region in Fig. 1), our IMTTS sample overlaps with the Herbig sample well, bridging the gap between the convective-radiative (CR) limit (thick blue line) and the radiative part of the HR diagram probed by the Herbig sample. Except for a small gap near the CR limit around $3 M_\odot$, the connection between partly convective IMTTS (green zone) and fully radiative IMTTS (blue zone) is fairly complete in our sample. In this region of the HR diagram, our study provides evidence of a very clear trend: convective stars quickly lose their magnetic field. Indeed, almost 100% (14 out of 15) of partly convective IMTTS host a magnetic field, while only $\sim 10\%$ (2 out of 18) of fully radiative IMTTS are magnetic, which is an occurrence similar to the fossil fields in the HAeBe and Ap/Bp stars. Furthermore, the non-magnetic star in the partly convective zone is NGC 2264 121, the one with a detection limit much larger than typical TTS magnetic fields. This star may well host a relatively strong magnetic field that we are not able to detect with our data due to its very rapid rotation.

The magnetic/non-magnetic boundary appears obvious in Fig. 1 and may define the boundary between ubiquitous dynamo-generated magnetic fields in convective stars and the rarer fossil magnetic fields in fully radiative stars. Stellar evolutionary grids from the CESAM code reveal that stars evolve across this boundary very quickly so that the transition between the two types of fields must occur within a few times 0.1 Myr. This timescale is similar to that found with the two other evolutionary PMS grids considered in this study. We thus propose that 0.1 Myr is the typical time-scale for dynamo fields to dissipate in IMTTS. In addition, we find that this transition occurs when $M_{\text{conv.env.}}/M_\star \sim 2\%$, or in terms of volume when $R_{\text{con.env.}}/R_\star \sim 25\%$.

Typical fossil fields detected in Ap/Bp stars have predominantly dipolar configurations and have dipole field strengths of a few kG (e.g. Donati & Landstreet 2009). Most of the detection limits we measured in our non-magnetic sample are lower than 1 kG, with the majority having a limit lower than 0.5 kG. Our data are therefore sensitive enough for detecting typical fossil fields.

This is true if we ignore the dilution effect of magnetic flux due to the radius variation during stellar evolution. The fossil field hypothesis assumes magnetic flux conservation implying that the magnetic strength at the stellar surface varies as $1/R_*^2$. As a consequence, magnetic fields are weaker at large radii. Between the birthline and the Terminal Age Main Sequence (TAMS), the radius changes the most during the early-PMS phase. However, between the CR limit (after which only fossil field can be present at the surface of the stars) and the ZAMS, the radius only changes by a factor of about 2, i.e. a similar factor between the TAMS and the ZAMS. Therefore, the dilution effect affects Ap/Bp stars and radiative PMS stars the same way, and can be neglected in our interpretation. In the fossil field approximation, the magnetic strength and topology we expect to detect in the radiative IMTTS are therefore likely of Ap/Bp type.

If our data are sensitive enough to detect Ap/Bp fields, by extension it should also be sensitive enough to detect "typical" Herbig Ae/Be fossil fields. We observe that our IMTTS dataset is more sensitive to magnetic field than the HAeBe dataset (Alecian et al. 2013). Indeed, 80% of our B_ℓ measurements have uncertainties below 50 G (see Table B.5), which is the case for only 20% of the HAeBe dataset, and 80% of it has uncertainties below 250 G. Nonetheless, fossil fields have been detected in the HAeBe sample (e.g. Alecian et al. 2013), which emphasises that our dataset is sensitive enough to detect fossil fields.

Fossil magnetic fields are present in 1 to 10% of the A/B stars, depending on the mass: while it is found to be 5-10% above $2.5 M_\odot$ it drops quickly to 1% below $2.5 M_\odot$ (Power et al. 2008; Sikora et al. 2018). According to the fossil field hypothesis, a similar incidence is expected in the PMS radiative stars. Two out of the 18 radiative IMTTS we observed are magnetic. This is in global agreement with the fossil field theory, regardless of the mass, and considering the small size of our sample. However, about 90% of our sample has masses concentrated between $\sim 1 M_\odot$ and $\sim 2.5 M_\odot$ (Fig. 1). Yet, the only magnetic fields we have detected in the radiative zone are in stars more massive than $3 M_\odot$. The absence of magnetic field detection in radiative stars less massive than $2.5 M_\odot$ is therefore striking. Our observations suggest that the incidence drop observed during the MS, is already present during the PMS phase.

While below $2.5 M_\odot$ there is a very distinct boundary between the magnetic and non-magnetic stars, above $3 M_\odot$ the boundary is not that evident. First, our sample does not contain any stars more massive than $3 M_\odot$ with a large outer convective envelope ($>0.25 R_*$). Secondly our sample contains in total only 3 stars more massive than $3 M_\odot$, which is not statistically significant. Nonetheless, if the two magnetic stars detected among those 3 have fossil fields, it would mean that we would have been lucky to detect them. It is probably more likely to assume that what we observe may be dynamo-fields created in the outer convective envelope, even if it contains less than 2% of the stellar mass or is contained in less than 25% of the stellar radius. The still open question would be to know whether it is possible to generate magnetic fields in such light but extended convective zones. Our data does not allow us to choose between simple and complex field for those stars. Additional observations are

required to determine the origin of their magnetic fields, and to better understand the origin of fossil fields in stars more massive than $3 M_\odot$.

4.2. Transition from fully convective to fully radiative

To better understand the evolution of magnetic fields during the PMS phases, we need to know their strengths and topologies. This requires good quality monitoring that necessitates a large amount of telescope time. This is currently being done on a sub-sample of our stars as a follow-up of this study.

In the mean time, with the spectropolarimetric snapshots we obtained, we studied the evolution of the mean longitudinal magnetic field B_ℓ . Mean longitudinal magnetic field measurements are not ideal because they vary significantly over the rotation of the star, but we can lessen this effect by choosing the highest absolute value amongst all observations of a particular star. As the star rotates, the B_ℓ values vary periodically, and the periodic curve depends on the field strength and topology. For a fixed topology the maximum absolute value ($|B_\ell|_{\max}$) increases with the magnetic strength. With only two to four observations we cannot draw the entire curve. We therefore chose the maximum measured absolute value as being the most representative value for the magnetic field's strength. In Table B.5, the $|B_\ell|_{\max}$ value of each star is indicated in bold: this value has been used to plot the size of the symbols in Fig 1.

In addition, from the shape of the LSD Stokes V profiles, we can begin to diagnose whether the Zeeman signature is most likely produced by a low-order field (simple bipolar signatures spread over the entire width of the I profile) or whether it is most likely produced by a complex multipolar field: composite and complex Stokes V signals often spread over only a small part of the width of the I profile, suggesting localised magnetic spots. For 10 out of the 16 magnetic IMTTS plotted in the HR diagram, we are able to say confidently that their magnetic field is complex, while only one star of our sample seems to host a simple magnetic field. The simple, complex and uncertain field natures are expressed in Fig. 1 with different symbols.

We found magnetic fields in only two radiative stars: CO Ori and GW Ori. They are our best candidates for hosting a fossil field. In addition, their B_ℓ are among the strongest detected in this sample (96.7 and 82.5 G, respectively) despite the relatively poor monitoring (only 2 spectra for CO Ori and 3 spectra for GW Ori). We tried to determine the complexity of their fields, but find their Stokes V profile time-series are difficult to interpret (see Fig B.3 for CO Ori and Fig B.7 for GW Ori). They are both excellent targets for future studies as they may host freshly formed fossil fields.

On the opposite side of the HR diagram, we note that IMTTS with large convective envelopes ($R > 0.40 R_*$) follow the same trend: most of the time, they host a multipolar or a multipolar+toroidal field. According to previous studies, including the magnetic mapping of the IMTTS CR Cha (Hussain et al. 2009), those multipolar and toroidal fields are indeed expected once the fully-convective limit (between the orange and green zone, see Fig. 1) is passed (Gregory et al. 2012).

The rest of the magnetic sample (all the partly convective stars with a weaker magnetic field, located closer to the convective radiative limit, with $R < 0.40 R_*$) is much more difficult to interpret because these stars have all kind of field complexities, with no apparent correlation with their degree of convection. For example, the Stokes V profiles of IRAS 22144 behave like a composite of multiple signals and could therefore hide a complex field (despite IRAS 22144 being almost entirely radiative)

while the more convective star CHX 22 profile seems of simpler configuration. Moreover, the B_l amplitudes of these stars do not show any correlation with the apparent complexity of their fields. It then appears to us that this region of the HR diagram (where $R_{\text{conv.env.}}$ evolves from 40 to 25% of R_{tot}) is a transition region between two regimes: the regime of strong and complex fields in highly convective stars (at the right of the HRD, where $R_{\text{conv.env.}} \geq 40\%$ of R_{tot}) and the regime of radiative IMTTS (at the left of the HRD, where $R_{\text{conv.env.}} \leq 25\%$ of R_{tot}) where more than 90% of the stars have either no field, or a field too faint to be detected with our observations.

Another interesting point can be mentioned: it may be possible that the magnetic IMTTS which do not evolve into Ap/Bp stars could be the progenitors of the weakly-magnetised "Vega-like" A stars (Lignières et al. 2009; Petit et al. 2010, 2011; Blazère et al. 2016b,a).

4.3. Low-mass T Tauri stars and the role of accretion

Magnetic fields are systematically detected in T Tauri stars. The discussion in Hill et al. (2017) compiles and summarises the magnetic properties of 16 TTS with masses ranging from 0.5 to 1.9 M_{\odot} , and ages ranging from 1 to 10 Myr (8 classical TTSs from the MaPP programme, 6 weak-line TTSs from the MaTYSSSE programme, and 2 additional weak-line TTSs from Hill et al. 2017). The 3 most massive stars in this study (Par 2244, Par 1379 and V410 Tau, at around 1.4 - 1.8 M_{\odot}) overlap with the lightest and most convective stars of our sample and display similar magnetic topologies.

Lavail et al. (2017) have measured the averaged modulus of the magnetic field over the visible stellar hemisphere ($\langle B \rangle$) of 6 IMTTS from the Zeeman broadening of IR spectral lines. When compared to LMTTS in which similar measurements have been performed, Lavail et al. (2017) proposed that we cannot find as strong magnetic fields in IMTTS as in some LMTTS. In Fig. 1, we observe that the stars with the strongest B_l (larger than 300 G) are the coolest TTS with effective temperatures lower than ~ 4000 K. These stars also have simple fields and are mainly convective. On the contrary, the TTS with the lowest longitudinal field values are slightly more evolved, and have complex fields. However, it does not mean that their total magnetic energy is lower because the cancellation effect affects B_l measurements, even more in the case of complex fields. It may just be that the lowest order dipole field component is weaker. Such a decrease of the dipole component with the decrease of the size of the convective envelope has already been noted by Gregory et al. (2012). In addition, we can compare B_l measurements of complex fields between our sample and the LMTTS. We observe they all have values of the same order of magnitude. Therefore our B_l data cannot confirm the trend found by Lavail et al. (2017) from mean field measurements: it is important to keep in mind that the two studies measured different kinds of magnetic field (global and local) that do not necessarily follow the same trend with mass.

Hill et al. (2017) also looked for correlation between magnetic topologies of LMTTS and their accretion state. While remaining cautious, they point out that wTTSs generally show a wider range of field topologies compared to cTTSs, with large-scale fields that can be more toroidal and non-axisymmetric. We looked for correlations between magnetic strengths / topologies and the accretion states of our sample of stars: from the accretion state (wTTS or cTTS) we compiled from the literature (Table B.2), we do not find any kind of correlation.

5. Conclusions

We have analysed spectropolarimetric data of a sample of 38 IMTTS probing the zone of the HRD where intermediate-mass stars evolve from a fully convective to a fully radiative internal structure. We have detected magnetic fields in about half of our sample. We find that the magnetic incidence goes from almost 100% to $\sim 10\%$ as soon as the stars cross the limit over which the convective zone has a mass lower than $\sim 2\%$ of the stellar mass, which is equivalent to $\sim 25\%$ of the stellar radius. We argue that dynamo fields have to dissipate within about few 0.1 Myr once this limit has been reached. We are however not able to constrain the time-scale over which they relax into fossil fields. Additional studies of the radiative magnetic IMTTS are required.

From the shape of the Zeeman signatures, we find that the stars of our sample with a convective envelope spreading over 40% to 99% of the stellar radius most likely host complex high-order magnetic fields, as observed among the low-mass TTS that are similarly convective. In addition, this may be evidence of a decrease in the low-order large-scale magnetic field component from the fully convective limit to the fully radiative limit, as in the LMTTS. We find no correlation between the magnetic signature shapes and strengths, and the accreting nature (wTTS or cTTS) of our IMTTS sample.

Acknowledgements

We are grateful to the referee for his judicious comments and to Silvia Alencar for her help and contribution. We acknowledge financial support from "Programme National de Physique Stellaire" (PNPS) of CNRS/INSU, France. This work was based on observations made with ESO Telescopes at the La Silla Paranal Observatory under Programme IDs 089.C-0796 & 090.C-0131, and is partly sponsored by the Swiss National Science Foundation (Project number 200020-172505). FG acknowledges financial support from the Centre National d'Études Spatiales (CNES). This work has made use of the VALD database, operated at Uppsala University, the Institute of Astronomy RAS in Moscow, and the University of Vienna, and of data from the European Space Agency (ESA) mission *Gaia* (<https://www.cosmos.esa.int/gaia>), processed by the *Gaia* Data Processing and Analysis Consortium (DPAC, <https://www.cosmos.esa.int/web/gaia/dpac/consortium>). Funding for the DPAC has been provided by national institutions, in particular the institutions participating in the *Gaia* Multilateral Agreement. Finally, we thank Aline Bellosguardo and the entire administrative team of IPAG for their excellent work and support.

References

- Alecian, E., Kochukhov, O., Neiner, C., et al. 2011, A&A, 536, L6
- Alecian, E., Tkachenko, A., Neiner, C., Folsom, C. P., & Leroy, B. 2016, A&A, 589, A47
- Alecian, E., Wade, G. A., Catala, C., et al. 2009, MNRAS, 400, 354
- Alecian, E., Wade, G. A., Catala, C., et al. 2013, MNRAS, 429, 1001
- Allard, F., Homeier, D., & Freytag, B. 2011, in Astronomical Society of the Pacific Conference Series, Vol. 448, 16th Cambridge Workshop on Cool Stars, Stellar Systems, and the Sun, ed. C. Johns-Krull, M. K. Browning, & A. A. West, 91
- Amard, L., Palacios, A., Charbonnel, C., Gallet, F., & Bouvier, J. 2016, A&A, 587, A105
- Angulo, C., Arnould, M., Rayet, M., et al. 1999, Nuclear Physics A, 656, 3
- Asplund, M., Grevesse, N., & Sauval, A. J. 2005, in Astronomical Society of the Pacific Conference Series, Vol. 336, Cosmic Abundances as Records of Stellar Evolution and Nucleosynthesis, ed. T. G. Barnes, III & F. N. Bash, 25
- Asplund, M., Grevesse, N., Sauval, A. J., & Scott, P. 2009, ARA&A, 47, 481

- Astraatmadja, T. L. & Bailer-Jones, C. A. L. 2016, *ApJ*, 833, 119
- Baxter, E. J., Covey, K. R., Muench, A. A., et al. 2009, *AJ*, 138, 963
- Behrend, R. & Maeder, A. 2001, *A&A*, 373, 190
- Blazère, A., Neiner, C., & Petit, P. 2016a, *MNRAS*, 459, L81
- Blazère, A., Petit, P., Lignières, F., et al. 2016b, *A&A*, 586, A97
- Böhm-Vitense, E. 1958, *ZAp*, 46, 108
- Boro Saikia, S., Jeffers, S. V., Morin, J., et al. 2016, *A&A*, 594, A29
- Braithwaite, J. & Spruit, H. C. 2004, *Nature*, 431, 819
- Casagrande, L., Ramírez, I., Meléndez, J., Bessell, M., & Asplund, M. 2010, *A&A*, 512, A54
- Charbonnel, C., Decressin, T., Lagarde, N., et al. 2017, *A&A*, 605, A102
- Crawford, I. A. 2000, *MNRAS*, 317, 996
- Cutri, R. M., Skrutskie, M. F., van Dyk, S., et al. 2003, *VizieR Online Data Catalog*, 2246
- Da Rio, N., Robberto, M., Soderblom, D. R., et al. 2009, *ApJS*, 183, 261
- de Zeeuw, P. T., Hoogerwerf, R., de Bruijne, J. H. J., Brown, A. G. A., & Blaauw, A. 1999, *AJ*, 117, 354
- Donati, J.-F. 2003, in *Astronomical Society of the Pacific Conference Series*, Vol. 307, *Solar Polarization*, ed. J. Trujillo-Bueno & J. Sanchez Almeida, 529
- Donati, J.-F., Bouvier, J., Walter, F. M., et al. 2011a, *MNRAS*, 412, 2454
- Donati, J.-F., Gregory, S. G., Alencar, S. H. P., et al. 2011b, *MNRAS*, 417, 472
- Donati, J.-F., Gregory, S. G., Alencar, S. H. P., et al. 2013, *MNRAS*, 436, 881
- Donati, J.-F., Gregory, S. G., Montmerle, T., et al. 2011c, *MNRAS*, 417, 1747
- Donati, J.-F., Hébrard, E., Hussain, G. A. J., et al. 2015, *MNRAS*, 453, 3706
- Donati, J.-F., Jardine, M. M., Gregory, S. G., et al. 2007, *MNRAS*, 380, 1297
- Donati, J.-F., Jardine, M. M., Gregory, S. G., et al. 2008, *MNRAS*, 386, 1234
- Donati, J.-F. & Landstreet, J. D. 2009, *ARA&A*, 47, 333
- Donati, J.-F., Semel, M., Carter, B. D., Rees, D. E., & Collier Cameron, A. 1997, *MNRAS*, 291, 658
- Donati, J.-F., Skelly, M. B., Bouvier, J., et al. 2010a, *MNRAS*, 409, 1347
- Donati, J.-F., Skelly, M. B., Bouvier, J., et al. 2010b, *MNRAS*, 402, 1426
- Ducourant, C., Teixeira, R., Périé, J. P., et al. 2005, *A&A*, 438, 769
- Duez, V. & Mathis, S. 2010, *A&A*, 517, A58
- Eggenberger, P., Meynet, G., Maeder, A., et al. 2008, *Ap&SS*, 316, 43
- Eggleton, P. P., Faulkner, J., & Flannery, B. P. 1973, *A&A*, 23, 325
- Emeriau, C. & Mathis, S. 2015, in *IAU Symposium*, Vol. 307, *New Windows on Massive Stars*, ed. G. Meynet, C. Georgy, J. Groh, & P. Stee, 373–374
- Ferguson, J. W., Alexander, D. R., Allard, F., et al. 2005, *ApJ*, 623, 585
- Folsom, C. P., Bagnulo, S., Wade, G. A., et al. 2012, *MNRAS*, 422, 2072
- Folsom, C. P., Wade, G. A., Kochukhov, O., et al. 2008, *MNRAS*, 391, 901
- Formicola, A., Imbriani, G., Costantini, H., et al. 2004, *Physics Letters B*, 591, 61
- Gaia Collaboration, Brown, A. G. A., Vallenari, A., et al. 2016, *ArXiv e-prints* [[arXiv:1609.04172](https://arxiv.org/abs/1609.04172)]
- Gaurat, M., Jouve, L., Lignières, F., & Gastine, T. 2015, *A&A*, 580, A103
- Gregory, S. G., Donati, J.-F., Morin, J., et al. 2012, *ApJ*, 755, 97
- Gustafsson, B., Edvardsson, B., Eriksson, K., et al. 2008, *A&A*, 486, 951
- Herbig, G. H. 1962, *Advances in Astronomy and Astrophysics*, 1, 47
- Hill, C. A., Carmona, A., Donati, J.-F., et al. 2017, *MNRAS*, 472, 1716
- Hussain, G. A. J., Collier Cameron, A., Jardine, M. M., et al. 2009, *MNRAS*, 398, 189
- Iglesias, C. A. & Rogers, F. J. 1996, *ApJ*, 464, 943
- Kharchenko, N. V. 2001, *Kinematika i Fizika Nebesnykh Tel.*, 17, 409
- Kochukhov, O. 2015, *A&A*, 580, A39
- Kochukhov, O., Makaganiuk, V., & Piskunov, N. 2010, *A&A*, 524, A5
- Kounkel, M., Megeath, S. T., Poteet, C. A., Fischer, W. J., & Hartmann, L. 2016, *VizieR Online Data Catalog*, 182
- Krautter, J., Wichmann, R., Schmitt, J. H. M. M., et al. 1997, *A&AS*, 123, 329
- Lagarde, N., Decressin, T., Charbonnel, C., et al. 2012, *A&A*, 543, A108
- Landstreet, J. D. 1988, *ApJ*, 326, 967
- Lavail, A., Kochukhov, O., Hussain, G. A. J., et al. 2017, *A&A*, 608, A77
- Lignières, F., Petit, P., Böhm, T., & Aurière, M. 2009, *A&A*, 500, L41
- Luhman, K. L. & Mamajek, E. E. 2012, *ApJ*, 758, 31
- Maia, F. F. S., Corradi, W. J. B., & Santos, Jr., J. F. C. 2010, *MNRAS*, 407, 1875
- Manoj, P., Bhatt, H. C., Maheswar, G., & Muneer, S. 2006, *ApJ*, 653, 657
- Marques, J. P., Goupil, M. J., Lebreton, Y., et al. 2013, *A&A*, 549, A74
- Meynet, G. & Maeder, A. 1997, *A&A*, 321, 465
- Morel, P. & Lebreton, Y. 2008, *Ap&SS*, 316, 61
- Morin, J., Donati, J.-F., Petit, P., et al. 2010, *MNRAS*, 407, 2269
- Moss, D. 2001, in *Astronomical Society of the Pacific Conference Series*, Vol. 248, *Magnetic Fields Across the Hertzsprung-Russell Diagram*, ed. G. Mathys, S. K. Solanki, & D. T. Wickramasinghe, 305
- Palacios, A., Talon, S., Charbonnel, C., & Forestini, M. 2003, *A&A*, 399, 603
- Pecaut, M. J. & Mamajek, E. E. 2013, *ApJS*, 208, 9
- Petit, P., Dintrans, B., Solanki, S. K., et al. 2008, *MNRAS*, 388, 80
- Petit, P., Lignières, F., Wade, G. A., et al. 2011, *Astronomische Nachrichten*, 332, 943
- Petit, P., Lignières, F., Wade, G. A., et al. 2010, *A&A*, 523, A41
- Piskunov, N., Snik, F., Dolgoplov, A., et al. 2011, *The Messenger*, 143, 7
- Pols, O. R., Tout, C. A., Eggleton, P. P., & Han, Z. 1995, *MNRAS*, 274, 964
- Power, J., Wade, G. A., Aurière, M., Silvester, J., & Hanes, D. 2008, *Contributions of the Astronomical Observatory Skalnaté Pleso*, 38, 443
- Prugniel, P., Vauglin, I., & Koleva, M. 2011, *A&A*, 531, A165
- Rees, D. E. & Semel, M. D. 1979, *A&A*, 74, 1
- Richards, J. W., Starr, D. L., Miller, A. A., et al. 2012, *ApJS*, 203, 32
- Rogers, F. J. & Nayfonov, A. 2002, *ApJ*, 576, 1064
- Ryabchikova, T., Piskunov, N., Kurucz, R. L., et al. 2015, *Phys. Scr.*, 90, 054005
- Sikora, J., Wade, G. A., & Power, J. 2018, *Contributions of the Astronomical Observatory Skalnaté Pleso*, 48, 87
- Sousa, A. P., Alencar, S. H. P., Bouvier, J., et al. 2016, *A&A*, 586, A47
- Spangler, C., Sargent, A. I., Silverstone, M. D., Becklin, E. E., & Zuckerman, B. 2001, *ApJ*, 555, 932
- Sung, H., Chun, M.-Y., & Bessell, M. S. 2000, *AJ*, 120, 333
- Wade, G. A., Bagnulo, S., Kochukhov, O., et al. 2001, *A&A*, 374, 265
- Whittet, D. C. B., Prusti, T., Franco, G. A. P., et al. 1997, *A&A*, 327, 1194
- Xing, L. F. 2010, *ApJ*, 723, 1542
- Yu, L. F. & Donati, J.-F. 2017, in *SF2A-2017: Proceedings of the Annual meeting of the French Society of Astronomy and Astrophysics*, ed. C. Reylé, P. Di Matteo, F. Herpin, E. Lagadec, A. Lançon, Z. Meliani, & F. Royer, 69–72
- Zacharias, N., Monet, D. G., Levine, S. E., et al. 2004, in *Bulletin of the American Astronomical Society*, Vol. 36, *American Astronomical Society Meeting Abstracts*, 1418

Appendix A: PMS model influence

When placing a sample of stars in the HR diagram and when trying to determine their internal structure through stellar evolution laws, the considered evolutionary model takes a crucial role: the interpretation may vary from one model to another. We thus need to test different PMS evolutionary models. We compared three grids of PMS evolution models computed with the CESAM code, the Geneva Code, and the STAREVOL code. These three codes can describe the evolution of pre-main sequence stars in the range of mass we are interested in, and can thus be used to derive the internal structure of our stars.

Appendix A.1: The CESAM code

The CESAM grid has been computed by one of us (YL) with the CESAM code (Morel & Lebreton 2008) using a standard set of input physics: OPAL96 opacity tables (Iglesias & Rogers 1996) complemented at low temperatures by WICHITA data (Ferguson et al. 2005), OPAL2005 equation of state (Rogers & Nayfonov 2002), NACRE nuclear reaction rates (Angulo et al. 1999) except for the $^{14}\text{N}(p, \gamma)^{15}\text{O}$ reaction, where the LUNA rate (Formicola et al. 2004) was adopted, mixing-length theory of convection (Böhm-Vitense 1958), and outer boundary condition based on Eddington's grey atmosphere. Models do not include rotation, mass loss, element diffusion, convective core overshooting, or convective penetration of elements below the convective envelope. The AGSS09 solar mixture (Asplund et al. 2009) has been adopted. The initial parameters of the models (initial helium abundance Y_{ini} , metallicity $(Z/X)_{\text{ini}}$, and mixing-length parameter α) were fixed from the calibration of a solar model (i.e. a solar model that must have, at solar age, the observed solar luminosity, radius, and photospheric metallicity). This leads to $Y_{\text{ini}} = 0.2539$, $(Z/X)_{\text{ini}} = 0.01781$, $\alpha = 1.622$.

Appendix A.2: Geneva code

The Geneva code grid (Eggenberger et al. 2008, Haemmerlé 2014 PhD Thesis) has been computed by one of us (LH). Like the CESAM grid, that grid is calibrated on the sun, with no rotation, no mass loss, no diffusion, and no overshooting. The Geneva code grid is calculated with $Z_{\text{ini}} = 0.0122$, $Y_{\text{ini}} = 0.2485$, $\alpha = 1.6$, the equation of state and the opacity come both from OPAL (1996). Abundances are from Asplund et al. (2005), and the atmosphere model comes from Meynet & Maeder (1997).

Appendix A.3: The STAREVOL code

The STAREVOL grid has been computed by two of us (FG and LA). This grid is also calibrated on the sun, with no rotation, no mass loss, no diffusion, and no overshooting. They are calculated with $Z_{\text{ini}} = 0.0134$, $Y_{\text{ini}} = 0.2676$, $\alpha = 1.973$. The basic input physics (equation of state, nuclear reactions, opacities) can be found in Lagarde et al. (2012). The equation of state is based on the formalism developed by Eggleton et al. (1973) and extended by Pols et al. (1995). OPAL opacities from Iglesias & Rogers (1996) are complemented at low temperatures by atomic and molecular opacities of Ferguson et al. (2005). Abundances are from Asplund et al. (2005), and the atmosphere model is a PHOENIX atmosphere (Allard et al. 2011).

Appendix A.4: Comparison of the models

In Fig A.1., we overplotted and compared isomass evolutionary tracks for 1.2, 1.5, 2.0, 3.0 and 4.0 solar masses for these three PMS grids of models. Green lines correspond to the Geneva Code, red lines correspond to the STAREVOL code, and blue lines correspond to the CESAM code. Red dots are stars with a definite magnetic detection (DD), while black dots are stars in which no magnetic field has been detected (ND). We tried to find a boundary between the population of magnetic stars (on the right) and the population of non-magnetic stars (on the left) in terms of stellar internal structure (radius and/or mass of the convective envelope compared to the radius and/or mass of the radiative core). We figured out that these two populations of stars can be splitted by a bound marking the moment when the radiative core fills more than 70%-75% of the total radius of the star, which also matches the moment when the radiative core contains more than 99% of the total mass of the star. We propose to call this limit "the convective/radiative limit" (CR limit hereafter), i.e. the limit beyond which stars are almost entirely radiative and lose their dynamo field.

In the part of the HR diagram where our stars are located, we notice that the isomass evolutionary tracks are similar: the disparity from one model to another is always smaller than our smallest error bars on T_{eff} and L , meaning that the uncertainties on the stars' internal structure or characteristics are mainly due to our uncertainties on T_{eff} and L , and not on discrepancies between models. The same reasoning can be applied to the CR limits, all of them being located close to each other (the spread between them is smaller than the smallest error bars we have). We therefore can work with any of these three models, it wouldn't make any major difference in our interpretations. The biggest disagreement between these three models can be spotted at the very beginning of the evolutionary tracks, during the fully convective phase. This discordance comes from the atmosphere mode: the three models do not use the same outer boundary conditions. However, none of our stars are located in this region of the HR diagram, thus our interpretations shouldn't be impacted.

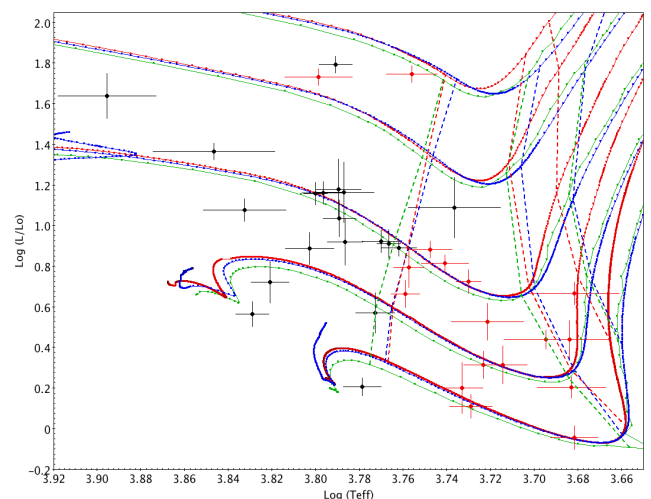


Fig. A.1. Blue tracks correspond to CESAM evolutionary models, red tracks to STAREVOL, and green tracks to the Geneva Code. Red dots are magnetic stars, while black dot are stars with no magnetic detection. The solid lines are (from bottom to top) 1.2, 1.5, 2.0, 3.0 and 4.0 M_{\odot} isomass evolutionary tracks. Dashed lines are (from right to left) $M_{\text{conv.}}/M_{\text{star}} = 99\%$, 50% and 1%.

Appendix B: LSD profiles

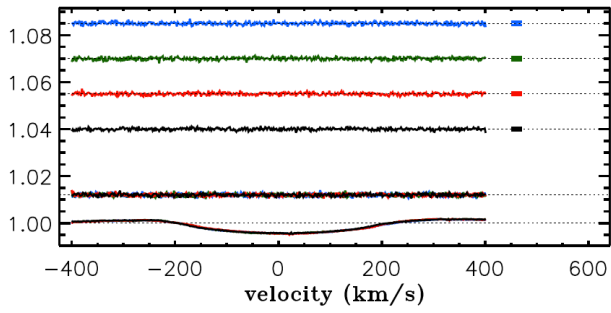


Fig. B.1. LSD profiles for BN Ori (no magnetic detection).

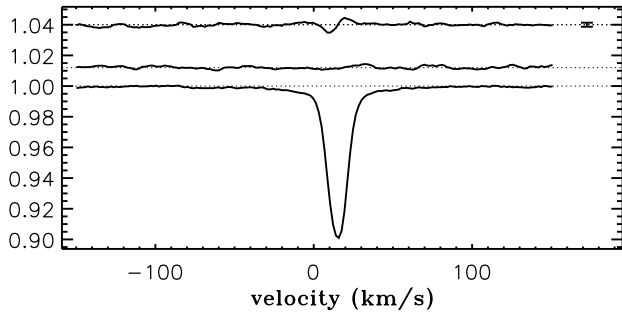


Fig. B.2. LSD profiles for CHX 22 (magnetic field detected, simple topology).

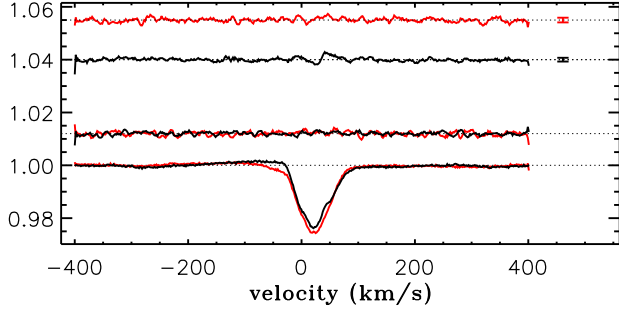


Fig. B.3. LSD profiles for CO Ori (magnetic field detected, uncertain topology).

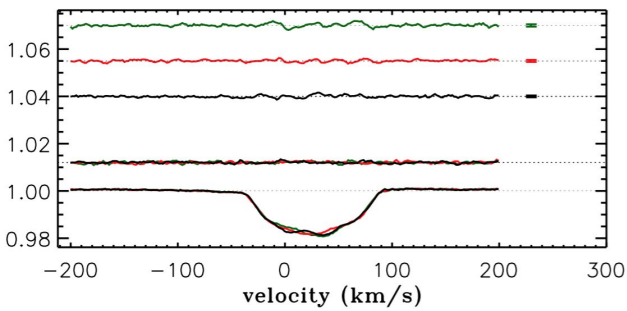


Fig. B.4. LSD profiles for COUP 1350 (magnetic field detected, complex topology).

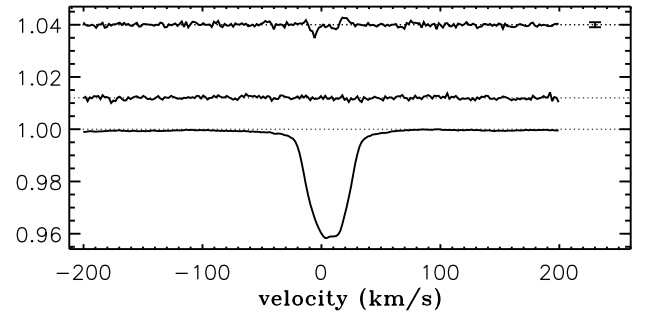


Fig. B.5. LSD profiles for CPD -43 7188 (magnetic field detected, complex topology).

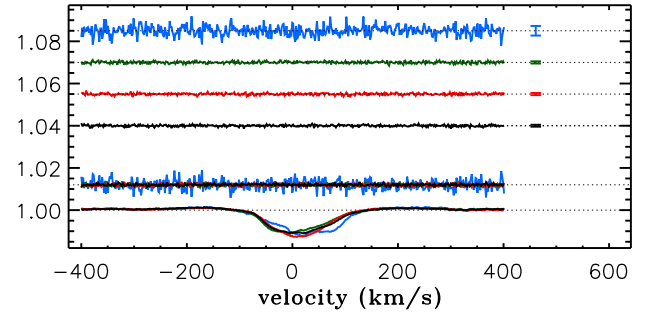


Fig. B.6. LSD profiles for CQ Tau (no magnetic detection).

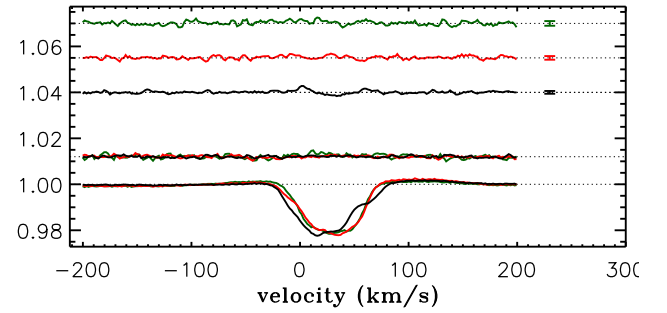


Fig. B.7. LSD profiles for GW Ori (magnetic field detected, uncertain topology).

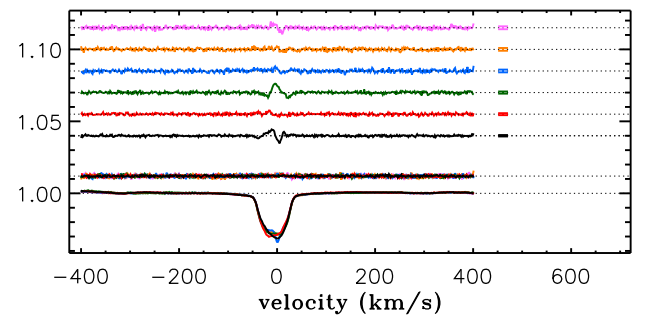


Fig. B.8. LSD profiles for HBC 741 (magnetic field detected, complex topology).

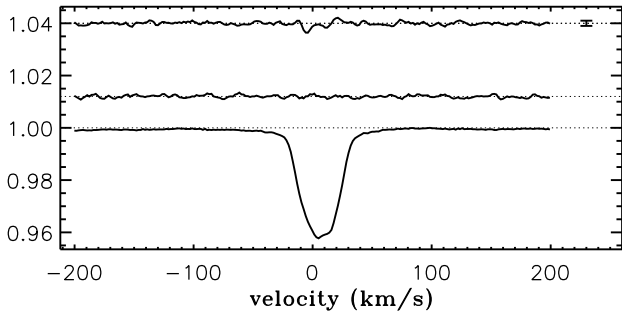


Fig. B.9. LSD profiles for HD 133938 (magnetic field detected, complex topology).

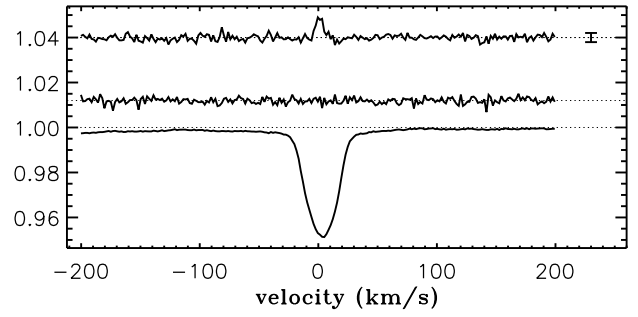


Fig. B.13. LSD profiles for HD 147048 (magnetic field detected, uncertain topology).

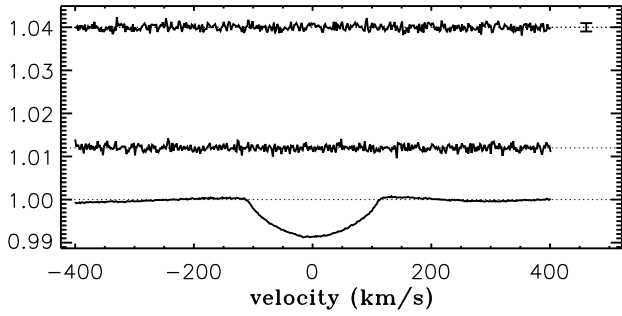


Fig. B.10. LSD profiles for HD 135127 (no magnetic detection).

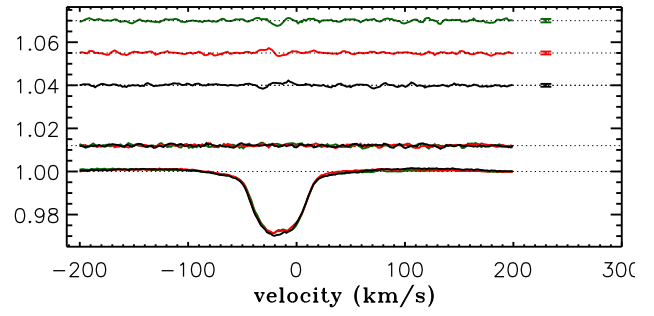


Fig. B.14. LSD profiles for IRAS 22144 + 6923 (magnetic field detected, complex topology).

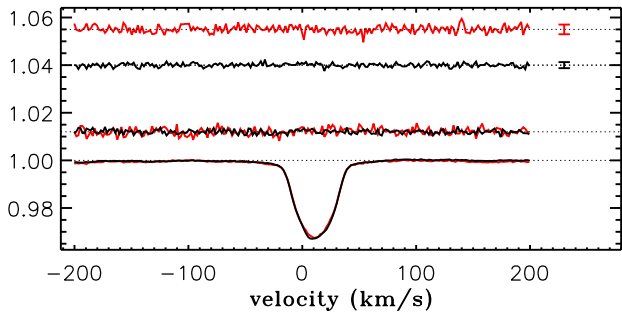


Fig. B.11. LSD profiles for HD 137059 (no magnetic detection).

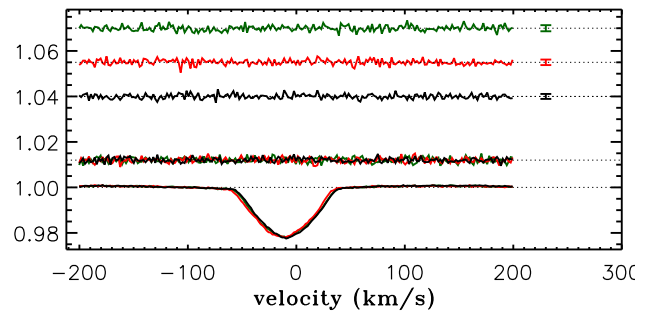


Fig. B.15. LSD profiles for IRAS 22152 + 6947 (no magnetic detection).

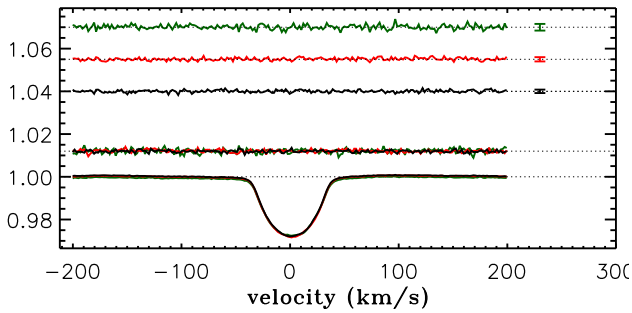


Fig. B.12. LSD profiles for HD 143978 (no magnetic detection).

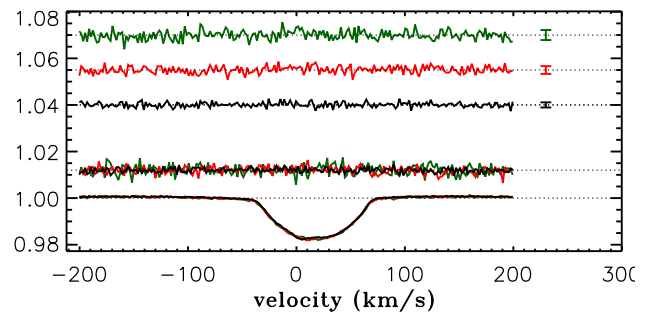


Fig. B.16. LSD profiles for NGC 2264 108 (no magnetic detection).

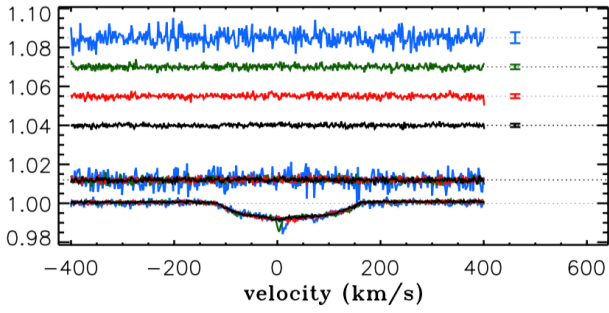


Fig. B.17. LSD profiles for NGC 2264 121 (no magnetic detection).

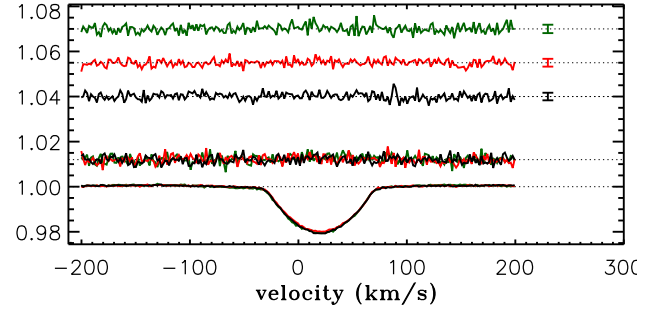


Fig. B.21. LSD profiles for Par 102 (no magnetic detection).

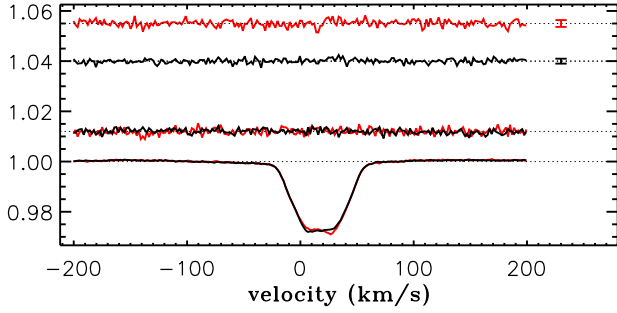


Fig. B.18. LSD profiles for NGC 2264 84 (no magnetic detection).

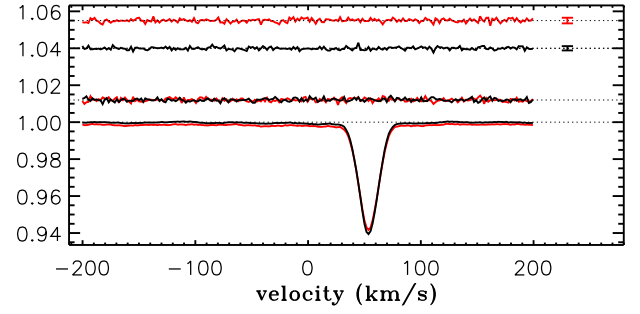


Fig. B.22. LSD profiles for Par 1391 (no magnetic detection).

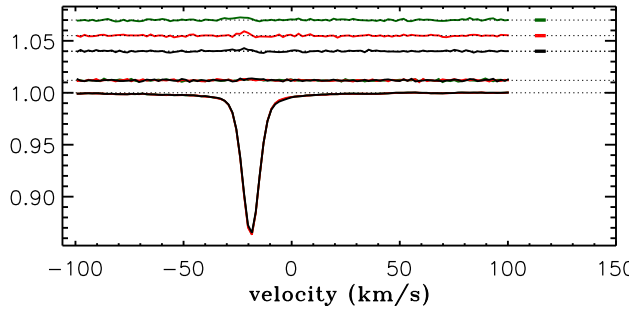


Fig. B.19. LSD profiles for NGC 6530 SCB 7 (magnetic field detected, uncertain topology).

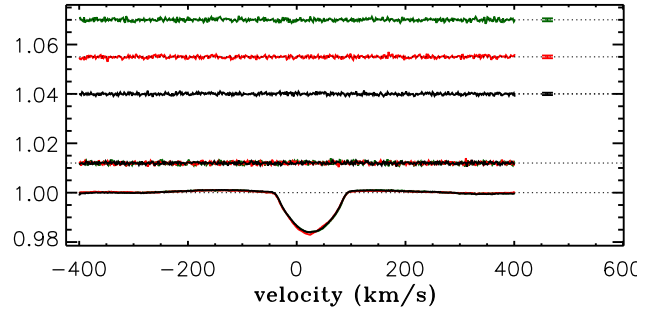


Fig. B.23. LSD profiles for Par 1394 (no magnetic detection).

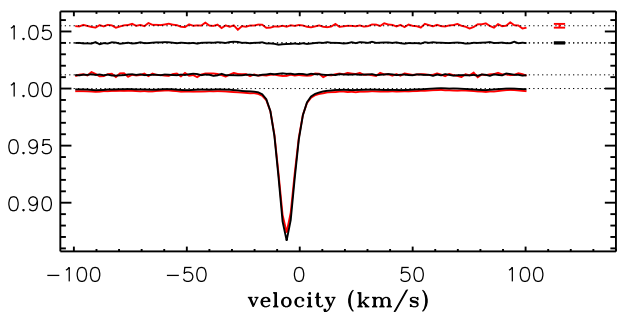


Fig. B.20. LSD profiles for NGC 6530 SCB 739 (no magnetic detection).

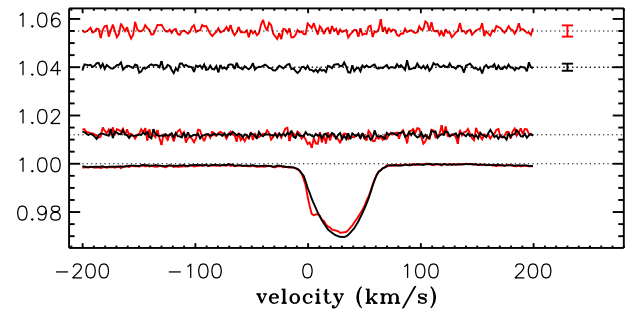


Fig. B.24. LSD profiles for Par 1414 (no magnetic detection).

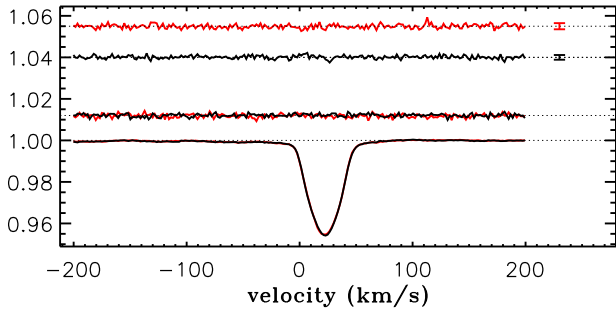


Fig. B.25. LSD profiles for Par 1455 (no magnetic detection).

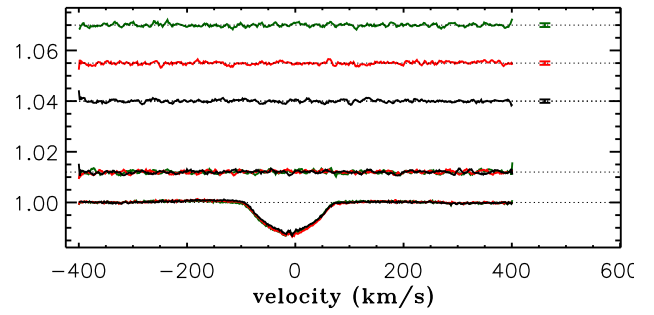


Fig. B.29. LSD profiles for PX Vul (no magnetic detection).

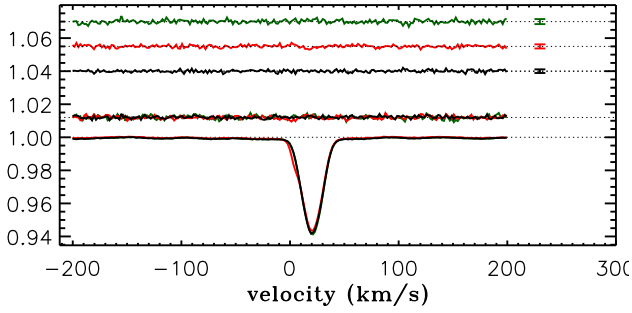


Fig. B.26. LSD profiles for Par 1646 (no magnetic detection).

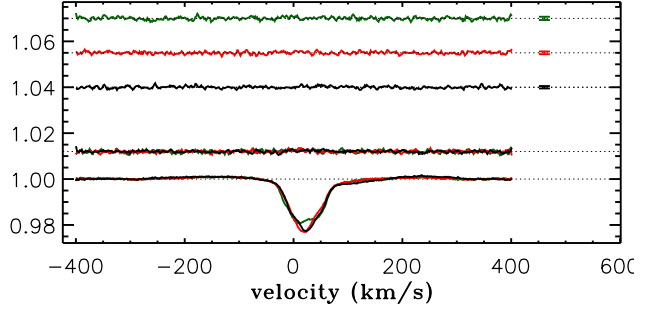


Fig. B.30. LSD profiles for RY Ori (no magnetic detection).

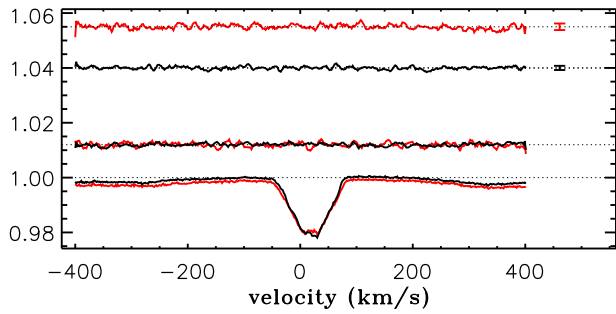


Fig. B.27. LSD profiles for Par 1736 (no magnetic detection).

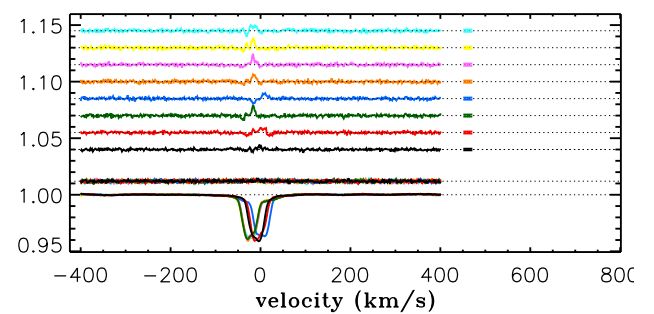


Fig. B.31. LSD profiles for V 1000 Sco (magnetic field detected, complex topology).

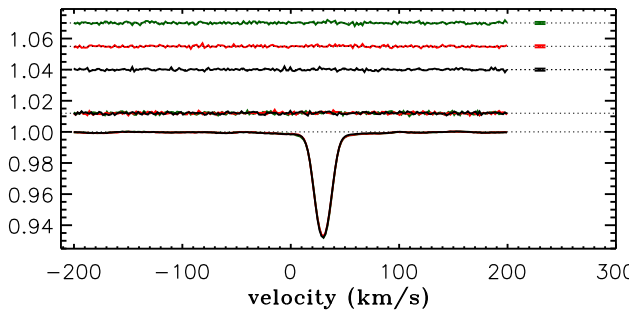


Fig. B.28. LSD profiles for Par 2441 (no magnetic detection).

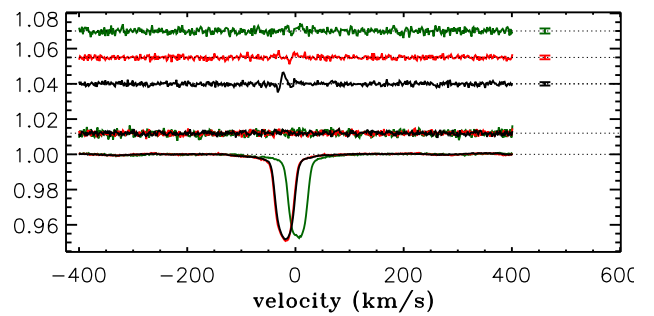


Fig. B.32. LSD profiles for V 1001 Sco (magnetic field detected, complex topology).

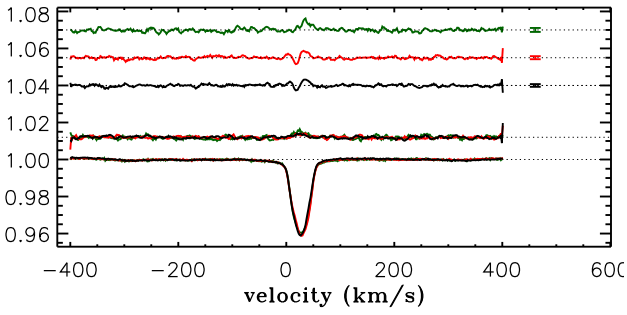


Fig. B.33. LSD profiles for V 1044 Ori (magnetic field detected, uncertain topology).

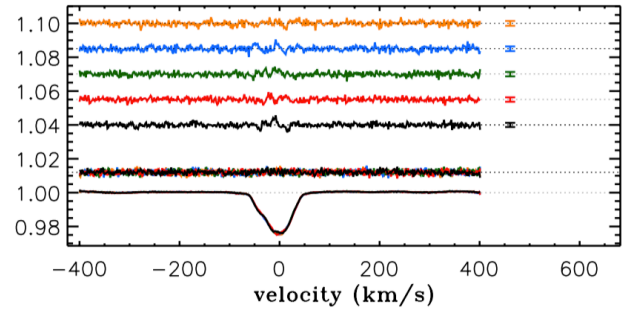


Fig. B.37. LSD profiles for V 1156 Sco (continued).

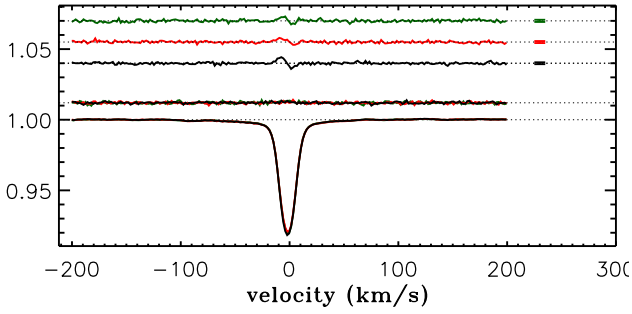


Fig. B.34. LSD profiles for V 1149 Sco (magnetic field detected, uncertain topology).

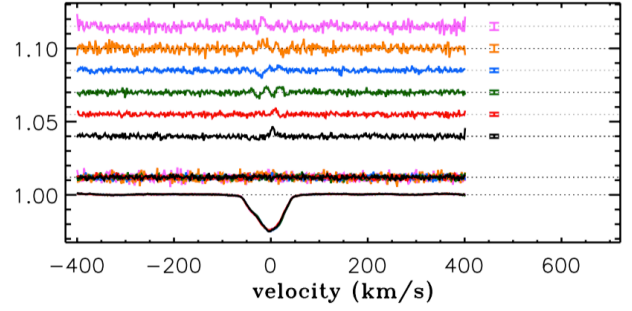


Fig. B.38. LSD profiles for V 1156 Sco (continued).

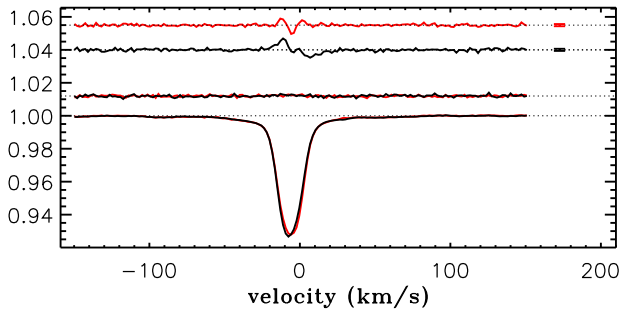


Fig. B.35. LSD profiles for V 1152 Sco (magnetic field detected, complex topology).

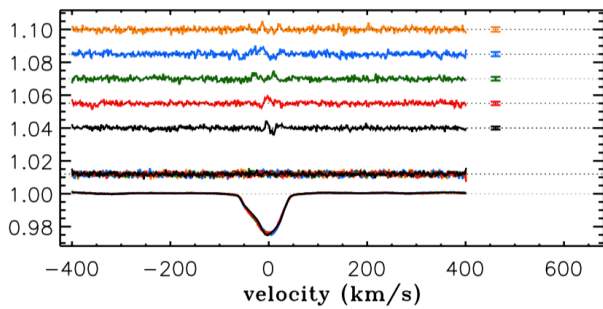


Fig. B.36. LSD profiles for V 1156 Sco (magnetic field detected, complex topology).

Table B.1. Log of the observations.

Target	Coordinates	Instrument	HJD (2450000+)	t_{exp} (s)	SNR (per ccd pxl)	SNR (LSD)
BN Ori	05 36 29.347 +06 50 02.17	ESPaDOnS	6196.01169	2160	340	18832
-			6272.05218	2160	290	15171
-			6286.08442	2160	315	16392
-			6293.85675	2160	325	17661
CHX 22	11 12 42.689 -77 22 23.05	HARPSpol	6140.48253	4800	55	3769
CO Ori	05 27 38.335 +11 25 38.92	ESPaDOnS	6197.00549	1560	170	7064
-			6284.80619	1560	145	5639
COUP 1350	05 35 26.202 -05 27 36.67	ESPaDOnS	6285.04068	4000	200	11450
-			6288.86765	4000	205	13249
-			6292.84744	4000	225	14480
CPD-43 7188	15 38 43.068 -44 11 47.42	HARPSpol	6128.60140	7200	90	10425
CQ Tau	05 35 58.467 +24 44 54.09	ESPaDOnS	6284.02976	6000	445	19472
-			6287.06958	6000	350	4382
-			6289.89715	6000	425	19086
-			6290.84611	6000	465	21871
GW Ori	05 29 08.391 +11 52 12.67	ESPaDOnS	6195.99311	480	200	11701
-			6258.12749	960	145	6981
-			6272.07160	480	165	8975
HBC 741	23 20 52.118 +74 14 07.10	ESPaDOnS	6100.12768	880	220	14587
-			6102.12400	880	205	13583
-			6104.11588	1760	305	19938
HD 133938	15 08 38.499 -44 00 51.97	HARPSpol	6140.56344	7200	75	7072
HD 135127	15 14 39.583 -34 45 41.31	HARPSpol	6131.52313	3152	110	10272
HD 137059	15 25 17.010 -38 45 25.88	HARPSpol	6129.49163	5600	50	4926
-			6131.57721	5600	70	7878
HD 143978	16 04 57.074 -38 57 15.71	HARPSpol	6129.70610	4000	115	12340
-			6130.55291	2800	95	10037
-			6130.63407	2800	60	6411
HD 147048	16 21 12.193 -40 30 20.59	HARPSpol	6131.65409	6704	50	4914
IRAS 22144	22 15 41.908 +69 38 56.69	ESPaDOnS	6100.10110	2640	175	10716
-			6101.08220	2640	145	9021
-			6103.02717	2640	165	10562
IRAS 22152	22 16 31.105 +70 02 39.35	ESPaDOnS	6100.10110	2640	175	9174
-			6101.08220	2640	145	7448
-			6103.02717	2640	165	8230
NGC 2264 108	06 40 51.185 +09 44 46.12	ESPaDOnS	6270.15205	3520	105	6008
-			6285.13122	3520	85	4670
-			6289.03847	3520	140	9062
NGC 2264 121	06 40 56.507 +09 54 10.42	ESPaDOnS	6267.16535	800	30	1066
-			6269.13658	800	55	2843
-			6286.11356	800	60	3465
-			6288.03579	800	50	2510
NGC 2264 84	06 40 42.183 +09 33 37.44	ESPaDOnS	6201.13037	2840	120	7375
-			6288.98198	5680	170	10222
NGC 6530 SCB7	18 03 22.59 -24 22 04.7	ESPaDOnS	6108.00466	1280	215	14153
-			6110.84930	1280	215	14131
-			6111.85859	1280	225	14845
NGC 6530 SCB739	18 04 36.103 -24 26 44.80	HARPSpol	6129.68867	8800	230	16375
-			6131.75909	2400	85	6062
PAR 102	05 29 11.440 -06 08 05.40	ESPaDOnS	6200.03445	440	105	5936
-			6284.82240	440	100	5777
-			6288.76243	440	95	5373
PAR 1391	05 34 15.196 -05 11 49.44	HARPSpol	6265.58358	5520	75	6545
-			6267.76109	6000	90	8617
PAR 1394	05 34 14.163 -05 36 54.25	ESPaDOnS	6284.94365	3120	325	18347
-			6288.79597	3120	275	21118
-			6200.08117	3120	285	16998
PAR 1414	05 34 21.377 -04 18 38.71	HARPSpol	6266.71310	12800	70	6768
-			6268.84148	7600	45	4302
PAR 1455	05 34 24.961 -05 22 05.53	HARPSpol	6265.64831	4800	75	6766
-			6267.63691	14400	95	8797
PAR 1646	05 34 55.208 -04 20 38.87	HARPSpol	6265.86174	3400	95	8997

-				6268.58229	4800	75	6568
-				6266.86804	3400	80	8031
PAR 1736	05 35 05.195 -05 14 50.34	HARPSpol		6265.72010	7200	100	6536
-				6268.65637	7200	70	4160
PAR 2441	05 36 51.270 -04 25 39.97	ESPaDOnS		6286.88901	2080	195	14347
-				6288.82923	2080	195	14536
-				6260.12791	2080	200	14457
PX Vul	19 26 40.250 +23 53 50.72	ESPaDOnS		6104.04050	2920	200	6679
-				6108.07777	2920	220	7356
-				6110.87961	2920	215	7322
RY Ori	05 32 09.942 -02 49 46.77	ESPaDOnS		6283.91923	5600	180	8169
-				6284.88690	5600	205	9706
-				6290.76770	5600	230	11095
V1000 Sco	16 11 08.908 -19 04 46.86	ESPaDOnS		5969.16094	2400	200	13827
-				6103.75536	2400	205	11784
V1001 Sco	16 11 59.272 -19 06 53.36	ESPaDOnS		5968.12625	1700	160	10412
-				5972.11674	1200	115	6970
-				6103.78273	1700	170	9340
V1002 Sco	16 12 40.516 -18 59 28.27	ESPaDOnS		5969.10633	6000	420	31570
-				6109.77816	6000	525	35521
V1044 Ori	05 34 16.462 -05 36 45.57	ESPaDOnS		6202.00591	760	100	6839
-				6271.11957	760	75	4660
-				6290.93247	760	90	6085
V1149 Sco	15 58 36.913 -22 57 15.22	ESPaDOnS		5967.09378	1000	180	13096
-				6099.78064	1000	225	14354
-				6101.78171	1000	240	15598
V1152 Sco	16 01 25.630 -22 40 40.29	ESPaDOnS		5968.16100	3040	190	15537
-				6102.75795	3040	210	15119
V1156 Sco	16 04 47.752 -19 30 22.92	ESPaDOnS		5968.09636	2800	260	21648
-				5972.09027	2800	200	15268

Table B.2. Table compiling stellar properties of our sample: effective temperature, projected rotational velocity, total radius of the star, mass, radius of the radiative core, convective turnover time at $\text{Hp}/2$ (at half a pressure scale height above the base of the convection zone), and accretion type. Error bars on T_{eff} and $v \sin i$ are detailed in Section 3.1.1., and error bars on the other parameters come from interpolations of the CESAM grids.

Identifier	T_{eff} (K)	$v \sin i$ (km/s)	Radius (R_{\odot})	Mass (M_{\odot})	$R_{\text{rad.core}}$ (R_{\odot})	$\log(\tau_c)$ (s)	Type	References for accretion type
BN Ori	7020 ± 450	214 ± 24	$3.250^{+0.476}_{-0.416}$	$2.149^{+0.130}_{-0.112}$	$3.221^{+0.427}_{-0.407}$	$4.304^{+0.673}_{-0.573}$		
CHX 22	5260 ± 200	9.87 ± 0.14	$2.204^{+0.300}_{-0.264}$	$1.772^{+0.168}_{-0.175}$	$1.378^{+0.141}_{-0.121}$	$6.690^{+0.168}_{-0.175}$	wTTS	Spangler et al. (2001)
CO Ori	6290 ± 220	69 ± 6	$6.174^{+0.543}_{-0.499}$	$3.225^{+0.175}_{-0.158}$	$5.958^{+0.355}_{-0.391}$	$4.434^{+0.760}_{-0.409}$	cTTS	Astraatmadja & Bailer-Jones (2016)
COUP 1350	5590 ± 130	61.8 ± 1.0	$2.934^{+0.201}_{-0.188}$	$2.099^{+0.144}_{-0.143}$	$2.099^{+0.112}_{-0.107}$	$6.415^{+0.152}_{-0.165}$		
CPD -43 7188	5360 ± 120	25.4 ± 0.5	$1.320^{+0.107}_{-0.099}$	$1.181^{+0.082}_{-0.074}$	$0.883^{+0.056}_{-0.055}$	$6.467^{+0.080}_{-0.083}$		
CQ Tau	6800 ± 290	94 ± 6	$2.491^{+0.278}_{-0.250}$	$1.747^{+0.101}_{-0.074}$	$2.451^{+0.191}_{-0.229}$	$3.697^{+0.965}_{-0.180}$		
CR Cha	4800 ± 230	34.5	$3.113^{+0.366}_{-0.327}$	$1.657^{+0.341}_{-0.413}$	$0.953^{+0.525}_{-0.953}$	$7.134^{+0.002}_{-4.133}$	cTTS	Hussain et al. (2009)
GW Ori	5700 ± 150	46.0 ± 1.6	$7.651^{+0.568}_{-0.186}$	$3.751^{+0.189}_{-0.186}$	$6.316^{+0.350}_{-0.331}$	$5.991^{+0.247}_{-0.294}$	cTTS	Astraatmadja & Bailer-Jones (2016)
HBC 741	5470 ± 70	40.0 ± 0.8	$2.658^{+0.197}_{-0.183}$	$2.026^{+0.117}_{-0.105}$	$1.718^{+0.122}_{-0.108}$	$6.651^{+0.068}_{-0.069}$	cTTS	Ducourant et al. (2005)
HD 133938	5290 ± 110	20.40 ± 0.23	$1.714^{+0.154}_{-0.141}$	$1.459^{+0.108}_{-0.099}$	$1.106^{+0.079}_{-0.073}$	$6.592^{+0.085}_{-0.083}$	wTTS	Xing (2010)
HD 135127	6740 ± 120	108 ± 5	$1.401^{+0.113}_{-0.085}$	$1.403^{+0.023}_{-0.095}$	$1.316^{+0.119}_{-0.095}$	$4.656^{+0.023}_{-0.095}$	wTTS	Krautter et al. (1997)
HD 137059	5840 ± 70	27.9 ± 1.7	$2.786^{+0.243}_{-0.223}$	$1.913^{+0.125}_{-0.116}$	$2.171^{+0.201}_{-0.182}$	$6.077^{+0.099}_{-0.109}$	wTTS	Xing (2010)
HD 143978	6010 ± 120	36.1 ± 0.8	$1.171^{+0.077}_{-0.072}$	$1.138^{+0.024}_{-0.107}$	$0.929^{+0.049}_{-0.123}$	$5.946^{+0.122}_{-0.112}$	wTTS	Xing (2010)
HD 147048	5410 ± 120	21.54 ± 0.41	$1.433^{+0.231}_{-0.199}$	$1.256^{+0.164}_{-0.141}$	$0.962^{+0.141}_{-0.120}$	$6.461^{+0.096}_{-0.092}$		
IRAS 22144 + 6923	5720 ± 90	34.9 ± 1.0	$2.541^{+0.316}_{-0.281}$	$1.842^{+0.173}_{-0.159}$	$1.883^{+0.248}_{-0.217}$	$6.261^{+0.111}_{-0.119}$		
IRAS 22152 + 6947	6620 ± 130	43.7 ± 2.4	$1.744^{+0.231}_{-0.204}$	$1.423^{+0.071}_{-0.071}$	$1.625^{+0.216}_{-0.216}$	$4.749^{+0.306}_{-0.337}$		
NGC 2264 108	6130 ± 200	52.6 ± 1.8	$3.387^{+0.675}_{-0.563}$	$2.108^{+0.296}_{-0.253}$	$2.939^{+0.607}_{-0.500}$	$5.509^{+0.348}_{-0.467}$	cTTS	Sousa et al. (2016)
NGC 2264 121	5450 ± 260	144 ± 12	$3.922^{+0.841}_{-0.693}$	$2.628^{+0.373}_{-0.405}$	$2.697^{+0.559}_{-0.454}$	$6.581^{+0.321}_{-0.369}$		
NGC 2264 84	6160 ± 140	36.3 ± 0.7	$3.407^{+0.652}_{-0.548}$	$2.113^{+0.281}_{-0.243}$	$2.986^{+0.620}_{-0.510}$	$5.433^{+0.287}_{-0.363}$	cTTS	Sousa et al. (2016)
NGC 6530 SCB 7	5490 ± 70	5.00 ± 0.22						
NGC 6530 SCB 739	6400 ± 100	4.28 ± 0.42						
Par 102	6160 ± 100	49.3 ± 1.5	$2.894^{+0.334}_{-0.300}$	$1.889^{+0.154}_{-0.136}$	$2.495^{+0.304}_{-0.269}$	$5.518^{+0.185}_{-0.221}$		
Par 1391	6350 ± 160	14.99 ± 0.47	$2.293^{+0.248}_{-0.223}$	$1.607^{+0.115}_{-0.095}$	$2.045^{+0.210}_{-0.191}$	$5.215^{+0.318}_{-0.391}$		
Par 1394	6260 ± 140	62.9 ± 1.7	$3.236^{+0.258}_{-0.239}$	$2.032^{+0.119}_{-0.106}$	$2.906^{+0.213}_{-0.199}$	$5.204^{+0.312}_{-0.384}$		
Par 1414	5920 ± 120	33.9 ± 1.0	$1.830^{+0.233}_{-0.207}$	$1.416^{+0.131}_{-0.113}$	$1.415^{+0.181}_{-0.158}$	$6.021^{+0.147}_{-0.163}$		
Par 1455	5890 ± 120	23.5 ± 0.6	$2.781^{+0.215}_{-0.199}$	$1.895^{+0.128}_{-0.113}$	$2.201^{+0.161}_{-0.150}$	$6.006^{+0.165}_{-0.180}$		
Par 1646	6310 ± 80	15.67 ± 0.39	$3.174^{+0.227}_{-0.211}$	$2.001^{+0.099}_{-0.092}$	$2.886^{+0.210}_{-0.198}$	$5.096^{+0.190}_{-0.236}$		
Par 1736	6180 ± 110	55.3 ± 2.6	$6.861^{+0.416}_{-0.392}$	$3.459^{+0.135}_{-0.134}$	$6.504^{+0.363}_{-0.333}$	$4.775^{+0.375}_{-0.423}$		
Par 2441	5780 ± 110	13.40 ± 0.39	$2.780^{+0.172}_{-0.162}$	$1.936^{+0.116}_{-0.106}$	$2.119^{+0.114}_{-0.108}$	$6.171^{+0.140}_{-0.155}$		
PX Vul	7860 ± 410	81 ± 5	$3.556^{+0.632}_{-0.536}$	$2.494^{+0.257}_{-0.223}$	$3.515^{+0.624}_{-0.529}$	$5.330^{+0.127}_{-0.160}$		
RY Ori	6120 ± 110	49.7 ± 1.7	$2.562^{+0.368}_{-0.322}$	$1.746^{+0.172}_{-0.157}$	$2.160^{+0.329}_{-0.283}$	$5.640^{+0.189}_{-0.223}$	cTTS	Richards et al. (2012)
V 1000 Sco	4830 ± 200	25.8 ± 1.9	$2.369^{+0.343}_{-0.299}$	$1.606^{+0.168}_{-0.303}$	$1.075^{+0.193}_{-0.566}$	$7.023^{+0.099}_{-0.188}$	wTTS	Luhman & Mamajek (2012)
V 1001 Sco	5180 ± 130	24.6 ± 0.8	$1.782^{+0.223}_{-0.198}$	$1.512^{+0.136}_{-0.135}$	$1.115^{+0.108}_{-0.099}$	$6.671^{+0.106}_{-0.103}$	wTTS	Luhman & Mamajek (2012)
V 1002 Sco	4950 ± 220	76.7 ± 3.3	$2.260^{+0.244}_{-0.220}$	$1.697^{+0.073}_{-0.221}$	$1.195^{+0.100}_{-0.311}$	$6.917^{+0.186}_{-0.185}$		
V 1044 Ori	5500 ± 140	26.7 ± 0.8	$2.804^{+0.202}_{-0.188}$	$2.072^{+0.138}_{-0.149}$	$1.927^{+0.101}_{-0.094}$	$6.520^{+0.149}_{-0.166}$	cTTS	Da Rio et al. (2009)
V 1149 Sco	5740 ± 90	12.06 ± 0.23	$2.172^{+0.185}_{-0.170}$	$1.641^{+0.111}_{-0.102}$	$1.602^{+0.136}_{-0.124}$	$6.241^{+0.102}_{-0.107}$	cTTS	Luhman & Mamajek (2012)
V 1152 Sco	4800 ± 120	13.1 ± 0.7	$1.373^{+0.119}_{-0.110}$	$1.206^{+0.058}_{-0.066}$	$0.816^{+0.038}_{-0.039}$	$6.756^{+0.096}_{-0.088}$	wTTS	Prugniel et al. (2011)
V 1156 Sco	4820 ± 180	48.3 ± 3.2	$1.816^{+0.176}_{-0.160}$	$1.438^{+0.057}_{-0.107}$	$0.972^{+0.062}_{-0.136}$	$6.893^{+0.152}_{-0.139}$		

Table B.3. Table compiling the 38 IMTTS identifiers, the associations they belong to, and the distances estimations we found in the literature (sources are mentioned : Gaia-TGAS parallax whenever possible, otherwise the associated star forming region or cluster distance).

Main identifier	2MASS identifier	Association	Distance (pc)	Source
BN Ori	J 05362935 + 0650020	RSF1 (OriB)	388 ± 5	Kounkel et al. (2016)
CHX 22	J 11124268 - 7722230	Cha1	160 ± 15	Whittet et al. (1997)
CO Ori	J 05273833 + 1125389	IC1	388 ± 5	Kounkel et al. (2016)
COUP 1350	J 05352620 - 0527366	Ori Neb Clus	388 ± 5	Kounkel et al. (2016)
CPD -43 7188	J 15384306 - 4411474	Lupus	127 ± 6	GAIA
CQ Tau	J 05355845 + 2444542	Tau	160 ± 7	GAIA
CR Cha	J 10590699 - 7701404	Cha	188 ± 8	GAIA
GW Ori	J 05290838 + 1152126	Ori	388 ± 5	Kounkel et al. (2016)
HBC 741	J 23205208 + 7414071	Cep	188 ± 9	GAIA
HD 133938	J 15083849 - 4400519	Lup	166 ± 10	GAIA
HD 135127	J 15143959 - 3445412	Lup	132 ± 7	GAIA
HD 137059	J 15251700 - 3845261	Lup	150 ± 10	Crawford (2000)
HD 143978	J 16045707 - 3857157	Lup	96 ± 2	GAIA
HD 147048	J 16211219 - 4030204	Lup	147 ± 20	GAIA
IRAS 22144 + 6923	J 22154189 + 6938566	Cep (L1219)	392 ± 41	GAIA
IRAS 22152 + 6947	J 22163111 + 7002393	Cep (L1219)	376 ± 41	GAIA
NGC 2264 108	J 06405118 + 0944461	NGC 2264	913 ± 150	Baxter et al. (2009)
NGC 2264 121	J 06405650 + 0954104	NGC 2264	913 ± 150	Baxter et al. (2009)
NGC 2264 84	J 06404218 + 0933374	NGC 2264	913 ± 150	Baxter et al. (2009)
NGC 6530 SCB 7	J 18032258 - 2422046	NGC 6530	1800 ± 100	Sung et al. (2000)
NGC 6530 SCB 739	J 18043607 - 2426447	NGC 6530	1800 ± 100	Sung et al. (2000)
Par 102	J 05291144 - 0608054	Ori	342 ± 32	GAIA
Par 1391	J 05341519 - 0511494	Ori	388 ± 5	Kounkel et al. (2016)
Par 1394	J 05341416 - 0536542	Ori Neb Clus	388 ± 5	Kounkel et al. (2016)
Par 1414	J 05342137 - 0418387	NGC 1981	380 ± 17	Maia et al. (2010)
Par 1455	J 05342495 - 0522055	Ori	388 ± 5	GAIA
Par 1646	J 05345520 - 0420389	NGC 1981	388 ± 5	Kounkel et al. (2016)
Par 1736	J 05350519 - 0514503	Ori	388 ± 5	Kounkel et al. (2016)
Par 2441		Ori OB1c	388 ± 5	Kounkel et al. (2016)
PX Vul	J 19264025 + 2353508	R Vul R2	420 ± 50	Manoj et al. (2006)
RY Ori	J 05320993 - 0249467	Ori	362 ± 44	GAIA
V 1000 Sco	J 16110890 - 1904468	Upper Sco	145 ± 14	de Zeeuw et al. (1999)
V 1001 Sco		Sco-Cen	145 ± 14	de Zeeuw et al. (1999)
V 1002 Sco	J 16124051 - 1859282	Upper Sco	131 ± 4	GAIA
V 1044 Ori	J 05341646 - 0536455	Ori	388 ± 5	Kounkel et al. (2016)
V 1149 Sco	J 15583692 - 2257153	Sco	166 ± 10	GAIA
V 1152 Sco	J 16012563 - 2240403	Upper Sco	141 ± 7	GAIA
V 1156 Sco	J 16044776 - 1930230	Upper Sco	140 ± 5	GAIA

Table B.4. Table compiling photometric measurements found in the literature : magnitudes V B and J, bolometric corrections in J band, theoretical $(V-J)_o$ and A_J from Pecaut & Mamajek (2013), and the corresponding $\log(L/L_\odot)$ with their associated uncertainties.

Identifier	V	B	J	$(BC)_J$	$(V-J)_o$	A_V	$\log(L/L_\odot)$
BN Ori	8.80	10.04	8.604	0.67	0.68	0.000	1.364 ± 0.042
CHX 22	11.103	12.02	8.645	1.23	1.48	1.377	0.525 ± 0.091
CO Ori	10.30	12.33	7.983	0.95	1.00	1.858	1.731 ± 0.042
COUP 1350	11.78	12.46	9.703	1.13	1.28	1.123	0.880 ± 0.042
CPD -43 7188	10.28	11.03	8.805	1.21	1.40	0.106	0.111 ± 0.057
CQ Tau	10.0	10.78	7.926	0.73	0.73	1.894	1.077 ± 0.055
CR Cha	11.0	12.15	8.462	1.34	1.72	1.152	0.667 ± 0.054
GW Ori	10.10	10.83	7.698	1.12	1.26	1.610	1.746 ± 0.042
HBC 741	10.22	11.17	8.308	1.21	1.42	0.694	0.723 ± 0.058
HD 133938	10.54	11.17	8.950	1.19	1.39	0.281	0.315 ± 0.066
HD 135127	9.15	9.64	8.235	0.76	0.77	0.203	0.564 ± 0.061
HD 137059	8.75	9.42	7.410	1.03	1.12	0.310	0.911 ± 0.070
HD 143978	9.20	9.70	8.143	0.99	1.06	0.000	0.207 ± 0.044
HD 147048	10.482	11.45	8.964	1.18	1.37	0.210	0.199 ± 0.125
IRAS 22144 + 6923	11.60	12.40	9.875	1.08	1.19	0.755	0.794 ± 0.099
IRAS 22152 + 6947	11.39	11.77	10.196	0.79	0.80	0.555	0.721 ± 0.103
NGC 2264 108	11.88	12.42	10.744	0.95	1.00	0.190	1.163 ± 0.148
NGC 2264 121	12.47	13.33	10.783	1.18	1.365	0.455	1.088 ± 0.148
NGC 2264 84	12.01	12.57	10.759	0.95	1.00	0.355	1.177 ± 0.148
NGC 6530 SCB 7	10.583	11.578	8.721	1.16	1.33	0.748	2.547 ± 0.063
NGC 6530 SCB 739	8.644	9.234	7.428	0.85	0.87	0.487	3.156 ± 0.063
Par 102	10.39	11.02	9.030	0.95	1.00	0.506	1.035 ± 0.091
Par 1391	10.698	11.2	9.65	0.88	0.905	0.200	0.887 ± 0.078
Par 1394	10.219	10.697	8.993	0.91	0.95	0.390	1.161 ± 0.056
Par 1414	11.48	12.12	10.274	1.00	1.07	0.190	0.570 ± 0.098
Par 1455	10.88	11.8	9.588	1.03	1.12	0.242	0.923 ± 0.056
Par 1646	9.72	10.19	8.853	0.89	0.93	0.000	1.158 ± 0.056
Par 1736	11.246	12.141	8.166	0.95	1.00	2.932	1.791 ± 0.042
Par 2441	10.741	11.430	9.432	1.08	1.19	0.168	0.890 ± 0.042
PX Vul	11.83	12.57	9.324	0.35	0.41	2.955	1.639 ± 0.111
RY Ori	10.80	12.76	9.444	0.95	1.00	0.503	0.918 ± 0.113
V 1000 Sco	12.050	12.99	8.761	1.36	1.75	2.171	0.439 ± 0.093
V 1001 Sco	11.59	12.82	8.981	1.26	1.52	0.476	0.313 ± 0.093
V 1002 Sco	10.829	12.15	8.313	1.30	1.63	1.535	0.440 ± 0.048
V 1044 Ori	11.51	12.123	9.701	1.16	1.33	0.674	0.813 ± 0.042
V 1149 Sco	10.14	10.92	8.358	1.08	1.19	0.835	0.664 ± 0.066
V 1152 Sco	11.4	12.6	9.324	1.38	1.83	0.348	-0.044 ± 0.059
V 1156 Sco	11.254	12.43	8.875	1.36	1.75	0.887	0.204 ± 0.051

Table B.5. Table compiling the extracted B_l and associated σ_{B_l} for each spectrum. Stars with a magnetic detection are written in bold, and so is the B_l we retained for them (the maximum in absolute value among all spectra for one star).

Target	HJD (2450000+)	B_l (G)	σ_{B_l} (G)
BN Ori	6196.01169	19.2	149.5
-	6272.05218	-197.0	181.1
-	6286.08442	-12.0	169.4
-	6293.85675	206.6	158.0
CHX 22	6140.48253	-35.3	23.0
CO Ori	6197.00549	-96.7	48.0
-	6284.80619	-72.0	53.4
COUP 1350	6285.04068	-1.5	34.5
-	6288.86765	23.4	29.8
-	6292.84744	-20.9	28.7
CPD-43 7188	6128.60140	-30.5	13.7
CQ Tau	6284.02976	40.3	39.7
-	6287.06958	-22.9	170.3
-	6289.89715	31.8	45.4
-	6290.84611	-33.3	36.6
GW Ori	6195.99311	49.5	32.7
-	6258.12749	43.4	50.4
-	6272.07160	82.5	41.5
HBC 741	6100.12768	64.2	15.1
-	6102.12400	44.5	16.1
-	6104.11588	-13.2	10.0
-	7879.12462	60.5	21.0
-	7886.11933	37.4	21.1
-	7886.13035	37.5	20.2
HD 133938	6140.56344	-28.7	22.0
HD 135127	6131.52313	-129.9	110.9
HD 137059	6129.49163	42.3	37.3
-	6131.57721	33.3	22.3
HD 143978	6129.70610	-10.0	18.9
-	6130.55291	-18.8	22.9
-	6130.63407	-18.2	36.5
HD 147048	6131.65409	8.2	24.4
IRAS 22144	6100.10110	-14.4	19.2
-	6101.08220	4.0	22.9
-	6103.02717	-3.0	18.5
IRAS 22152	6100.10110	-16.5	36.8
-	6101.08220	29.1	45.5
-	6103.02717	-65.9	41.2
NGC 2264 108	6270.15205	50.9	67.1
-	6285.13122	4.3	85.1
-	6289.03847	28.7	45.1
NGC 2264 121	6267.16535	87.0	1266.2
-	6269.13658	152.5	481.8
-	6286.11356	516.6	411.9
-	6288.03579	-91.6	539.2
NGC 2264 84	6201.13037	-64.9	28.6
-	6288.98198	-16.0	20.8
NGC 6530 SCB7	6108.00466	10.2	3.6
-	6110.84930	9.8	3.3
-	6111.85859	14.9	3.4
NGC 6530 SCB739	6129.68867	0.9	3.1
-	6131.75909	-2.0	8.8
PAR 102	6200.03445	2.0	57.9
-	6284.82240	-2.1	61.3
-	6288.76243	44.8	63.6
PAR 1391	6265.58358	1.8	17.6
-	6267.76109	2.2	13.6
PAR 1394	6284.94365	-4.6	26.2
-	6288.79597	30.4	23.2
-	6200.08117	-19.7	28.8
PAR 1414	6266.71310	-27.7	28.4

-	6268.84148	45.2	45.8
PAR 1455	6265.64831	-11.4	20.6
-	6267.63691	19.0	15.8
PAR 1646	6265.86174	-3.8	11.6
-	6268.58229	4.3	15.7
-	6266.86804	5.4	13.4
PAR 1736	6265.72010	-46.0	59.9
-	6268.65637	-30.9	91.5
PAR 2441	6286.88901	-4.6	6.1
-	6288.82923	-4.7	6.0
-	6260.12791	-6.0	6.1
PX Vul	6104.04050	-120.9	106.8
-	6108.07777	1.0	102.3
-	6110.87961	-112.1	94.7
RY Ori	6283.91923	20.5	43.2
-	6284.88690	38.7	34.7
-	6290.76770	-67.9	29.4
V1000 Sco	5969.16094	-38.9	9.3
-	6103.75536	-55.4	11.5
-	7817.06600	-116.6	14.3
-	7879.09957	21.4	16.2
-	7879.83844	-23.6	18.4
-	7881.97665	10.6	16.5
-	7883.05611	48.5	16.4
-	7886.89840	59.2	18.7
V1001 Sco	5968.12625	-35.1	11.6
-	5972.11674	-12.5	18.0
-	6103.78273	-5.0	13.5
V1002 Sco	5969.10633	20.5	17.8
-	6109.77816	-27.2	16.7
V1044 Ori	6202.00591	-24.7	21.1
-	6271.11957	-60.5	31.9
-	6290.93247	-17.5	24.1
V1149 Sco	5967.09378	4.4	5.9
-	6099.78064	12.6	5.5
-	6101.78171	28.1	5.0
V1152 Sco	5968.16100	86.4	6.0
-	6102.75795	2.0	6.4
V1156 Sco	5968.09636	-13.0	15.1
-	5972.09027	-18.5	21.0
-	7881.83655	7.9	18.4
-	7882.00559	-0.8	16.9
-	7882.85852	20.8	22.3
-	7883.08725	-43.6	22.4
-	7905.81407	18.6	21.2
-	7906.03909	0.9	21.0
-	7906.75247	22.3	22.0
-	7906.98154	13.0	19.8
-	7907.75468	-66.6	18.3
-	7907.99062	-48.5	20.5
-	7908.87211	94.4	40.0
-	7908.90669	-26.2	41.3
-	7909.87012	-17.8	21.7
-	7910.81390	-2.0	18.5
